Journal of Materials Chemistry A

COMMUNICATION

View Article Online
View Journal | View Issue

Cite this: J. Mater. Chem. A, 2019, 7, 19676

Received 4th July 2019
Accepted 7th August 2019

DOI: 10.1039/c9ta07194f

rsc.li/materials-a

A two-dimensional semiconducting covalent organic framework with nickel(II) coordination for high capacitive performance†

Tao Li,[a] Wen-Da Zhang,[a] Yong Liu,[a] Yunxing Li,[a] Caikun Cheng,[a] Haiyan Zhu,[a] Xiaodong Yan,*[a] Zaijun Li*[a] and Zhi-Guo Gu*[ab]

Covalent organic frameworks (COFs) have attracted enormous attention due to their unique structures, good crystallinity, modifiable functional groups, and excellent chemical stability. Nevertheless, their low electrical conductivity impeded their potential usage in supercapacitors. Herein, a two-dimensional conductive covalent organic framework (**Ni-COF**) with a square-planar Ni(II) coordination geometry is developed. The electrical conductivity of **Ni-COF** powder and thin film is 1.3×10^{-2} and 1.2 S cm^{-1}, respectively. The highly conjugated skeleton, ordered porous structure and numerous redox centres contribute to a high specific capacitance of 1257 F g^{-1} at 1 A g^{-1} with 94% capacitance retention after 10 000 cycles. Meanwhile, the asymmetric supercapacitor (activated carbon//**Ni-COF**) shows a high capacitance of 417 F g^{-1} at 1 A g^{-1}, and an outstanding energy density of 130 W h kg^{-1} at a power density of 839 W kg^{-1}, outperforming previously reported COF electrode materials and even comparable to metal–organic framework systems. Thus, this study opens a new way to construct highly conductive structure-controllable COF electrode materials for supercapacitors.

Two-dimensional (2D) materials have attracted much attention due to their unique and fascinating physicochemical properties.[1–4] Owing to their relatively high surface area and unusual electronic properties, 2D materials, including metal dichalcogenides, metal oxides, metal carbides, *etc.*, have been widely studied as electrode materials for supercapacitors.[2–8] Recently, 2D covalent organic frameworks (COFs) and metal–organic frameworks (MOFs) have emerged as a new class of electrode materials for supercapacitors.[9–12] COFs and MOFs have a highly tunable pore structure and functional units. It is thus promising to design high-performance COF and MOF electrodes for supercapacitors. One of the major challenges is boosting their electrical conductivity without compromising their inherent structural characteristics.[13–15] To construct conductive COFs, much effort has been focused on introducing functional groups, such as 4-thiophenephenyl,[16] lithium imidazolate groups[17] and other functional units[18] into the framework skeleton. Recently, Xu *et al.* and Jeong *et al.* separately showed that the ionic conductivity of COFs can be highly improved by introducing Li^+-responsive groups onto the surface of the pore channels.[19,20] However, the electronic and ionic conductivity of these COFs are still limited, mainly ranging from 2.38×10^{-6} to 7.2×10^{-3} S cm^{-1}.[16–20] Therefore, new strategies need to be developed to construct COFs with high electrical conductivity for high pseudo-capacitance.

Examples of 2D conductive MOFs in applications of supercapacitors have been demonstrated. A redox-active conductive 2D MOF with an exceptionally high volumetric capacitance of 760 F cm^{-3} and a high areal capacitance of 20 F cm^{-2} was constructed based on hexaaminobenzene linkers and metal ions (Ni^{2+} or Cu^{2+}).[21] Sheberla and co-authors reported on a highly conductive MOF, $[Ni_3(HITP)_2]_n$ (HITP = 2,3,6,7,10,11-hexaiminotriphenylene), with high electrical conductivity (50 s cm^{-1}) and high areal capacitance.[22] $Ni_3(HITP)_2$ is composed of π-conjugated 2D layers, and each layer is constructed from HITP molecules and Ni^{2+} linkers. The high conductivity could be ascribe to the planar Ni(II) coordination. Inspired by this, we aim to design a 2D COF with a highly conjugated structure and metal coordination. Herein, a conductive 2D Ni-containing covalent organic framework (**Ni-COF**) is thus designed and synthesized for high-performance supercapacitors. The Ni(II)-Salphen units, accompanied by the π-conjugation, favour the formation of a planar structure, contributing to the 2D layered structure. The temperature-dependent electrical conductivity revealed that **Ni-COF** behaves as a semiconductor at room temperature. The high conductivity and high-density active sites result in remarkable capacitance and excellent cycling stability.

[a]*Key Laboratory of Synthetic and Biological Colloids, Ministry of Education, School of Chemical and Material Engineering, Jiangnan University, Wuxi 214122, China. E-mail: xiaodong.yan@jiangnan.edu.cn; zaijunli@263.net; zhiguogu@jiangnan.edu.cn; Fax: +86 510 85917763; Tel: +86 510 85917090*

[b]*International Joint Research Center for Photoresponsive Molecules and Materials, School of Chemical and Material Engineering, Jiangnan University, Wuxi 214122, China*

† Electronic supplementary information (ESI) available: Experimental details, general characterization, additional plot and discussion. See DOI: 10.1039/c9ta07194f

Ni-COF was solvothermally synthesized by reacting 1,2,4,5-benzenetetraamine (BTA) and 2,5-dihydroxy-1,4-benzenedicarboxaldehyde (HBC) with $Ni(OAc)_2 \cdot 4H_2O$ at 120 °C for 3 days in a mixed solvent of mesitylene and 1,4-dioxane (Fig. 1a). The formation of Ni(II)-Salphen units can compete with the aldehyde-amino Schiff-base reaction, which would likely slow down the nucleation and result in a crystalline COF. **Ni-COF** shows good chemical and thermal stability. No decomposition and dissolution were detected by soaking in boiling water, 3 M HCl, 3 M KOH and common organic solvents for 5 days (Fig. S1†). TGA analysis confirmed the negligible weight loss below 250 °C (Fig. S2†).

PXRD analysis was used to demonstrate the structure of **Ni-COF**. As shown in Fig. 1b, the strong peak at 6.8° is attributed to the (100) facet, while the minor peaks at 8.5, 9.0 10.8 and 25.5° are attributed to (200), (210), (220) and (001) facets, respectively.[23] The presence of the (001) plane indicates π–π layered stacking.[24] The experimental PXRD pattern agreed well with the simulated pattern based on the eclipsed stacking model, and the unit cell parameters were calculated ($a = 13.5094$ Å, $b = 13.2250$ Å, $c = 24.1050$ Å, $\alpha = 25.6050$, $\beta = 32.1431$, and $\gamma = 55.6497$) with acceptable residuals ($R_p = 5.37\%$ and $R_{wp} = 6.23\%$). Ni(II) coordinates to two nitrogen atoms and two oxygen atoms. The N–Ni–N angle is 87° and the O–Ni–O angle is 91°, resulting in a square-planar Ni(II) coordination geometry. Six Ni(II)-Salphen units as the apexes are connected through alternately sharing the benzene rings of benzenetetraamine benzenedihydroxy, which form a hexagonal macrocycle (Fig. 1c). These π-conjugated Salphen hexagons are further extended to generate a 2D honeycomb-like layer structure. The shortest intralayer Ni···Ni distance is 7.6 Å, resulting in hexagonal pores with a pore size of 1.0 nm and a wall thickness of 0.3 nm. In addition, the pore-to-pore distance was calculated by using the Bragg equation according to the peak at 6.8°. It is 1.3 nm, which is consistent with the sum of pore diameters and wall thicknesses. It is noted that **Ni-COF** has a high Ni content of 17.6 wt%. From the simulated powder X-ray diffraction patterns, **Ni-COF** is verified to have a layered structure through an eclipsed stacking AA model with an interlayer separation of 3.4 Å (Fig. 1d).

According to the FT-IR spectra, the C–O stretching vibration of HBC at 1282 cm^{-1} shifts to 1295 cm^{-1} for **Ni-COF** (Fig. 2a), but is located at a similar place (1281 cm^{-1}) for the COF without Ni^{2+} (Fig. S3†). The shift thus could be ascribed to the Ni(II) coordination. The appearance of a signal from C=N (1621 cm^{-1}) and the concomitant disappearance of the characteristic N–H stretching vibration (3389–3197 cm^{-1}) and the C=O stretching band (1654 cm^{-1}) demonstrated the formation of Ni(II)-Salphen units (Fig. 2a).[25,26] The ^{13}C CP/MAS NMR spectrum of **Ni-COF** further reveals the presence of C=N and C–O groups (Fig. 2b and S4†). The resonance signals of C=N and C-O for the COF without Ni^{2+} appear at 173 and 156 ppm, respectively. However, the corresponding peaks of **Ni-COF** shift to 171 and 158 ppm, respectively, due to the effect of Ni(II) coordination.[27,28] These results confirm the formation of **Ni-COF**. SEM images show that **Ni-COF** possesses a spherical flower-like morphology, which is composed of numerous sheets (Fig. 2c and d, S5†). TEM images of **Ni-COF** show optically translucent features and a layered structure (Fig. 2e and f, S6†). The EDS mapping images reveal that the C, N, O and Ni elements in the selected area are uniformly distributed (Fig. 2g). The XPS survey of **Ni-COF** also confirms the presence of C, N, O and Ni. The signals at 399 and 532 eV correspond to N 1s and O 1s, respectively.[29] The Ni 2p spectrum exhibits two main peaks around 856.1 and 873.6 eV which are assigned to Ni $2p_{3/2}$ and Ni $2p_{1/2}$, respectively, together with their corresponding satellites around 861.3 and 880.1 eV, respectively (Fig. S7†).[30,31]

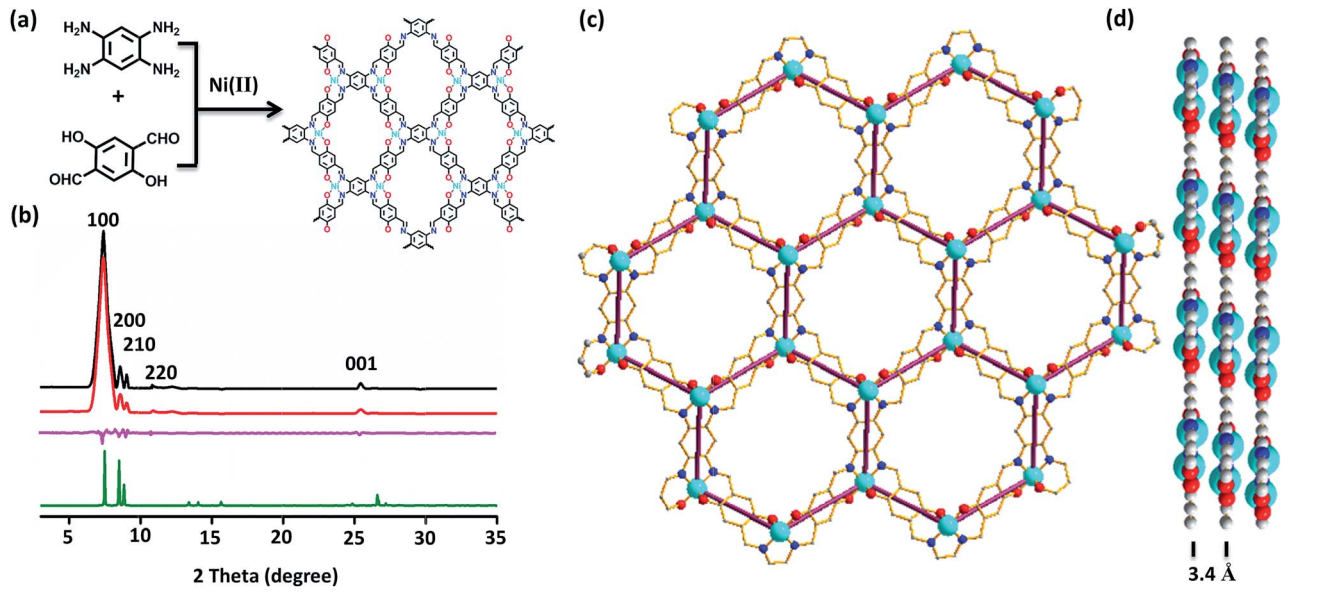

Fig. 1 (a) Synthetic scheme of Ni-COF. (b) PXRD patterns of Ni-COF with the experimental profiles in black, Pawley-refined profiles in red, calculated profiles in green, and the differences between the experimental and refined PXRD patterns in pink. (c) The stick model with regular microporous (d) Simulated structure with a 2D eclipsed layered arrangement.

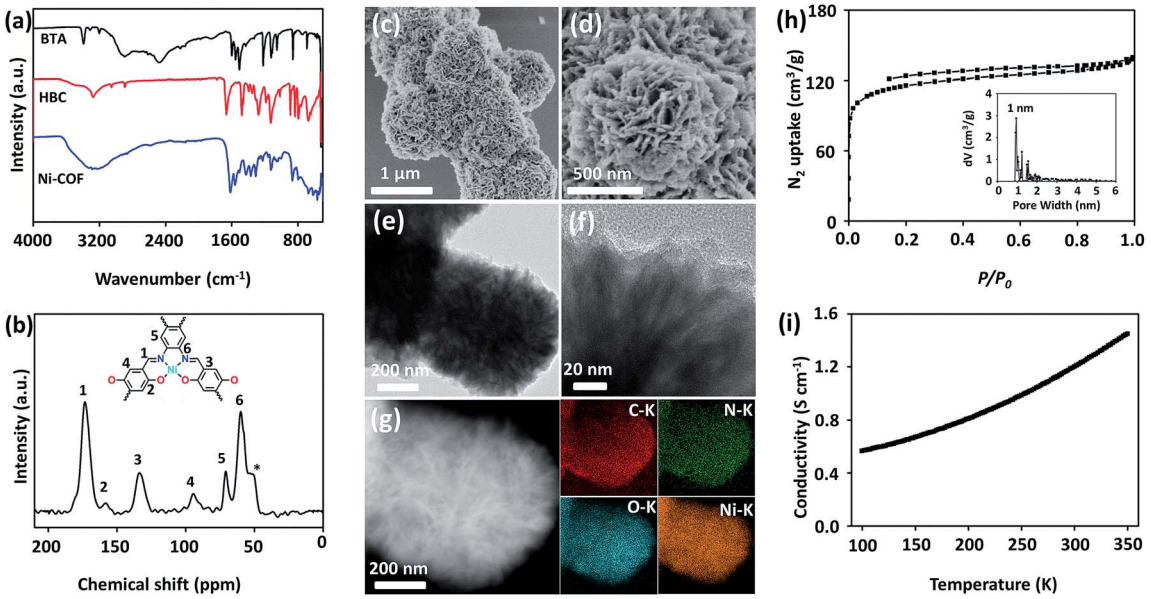

Fig. 2 (a) FT-IR spectra of BTA, HBC and **Ni-COF**. (b) Solid-state ^{13}C NMR spectrum of **Ni-COF**. (c and d) SEM images of **Ni-COF**. (e and f) TEM images of **Ni-COF**. (g) STEM image of **Ni-COF** and the corresponding elemental mapping spectra of C, N, O and Ni elements. (h) Nitrogen adsorption–desorption isotherm of **Ni-COF**, and the inset exhibits the pore size distribution. (i) Variable-temperature van der Pauw conductivity measurement.

The N_2 sorption isotherm of **Ni-COF** is a type I isotherm with a sharp N_2 uptake at low relative pressures ($P/P_0 < 0.01$), which indicates its microporous nature (Fig. 2h, S8 and S9†).[32] The BET surface area of **Ni-COF** was calculated to be 362 $m^2\ g^{-1}$. The pore size distribution was computed by using nonlocal density functional theory. The pore size distribution was concentrated at 1–1.6 nm, which is consistent with the simulated pore diameter.

To explore the effect of Ni(II) on electrical conductivity, a COF without Ni^{2+} (**Ni_0-COF**) was synthesized for comparison (Fig. S10–S16†). The electrical conductivity of **Ni-COF** powder was measured to be 1.3×10^{-2} S cm^{-1}, which is more than 1500 times that of **Ni_0-COF** (8.4×10^{-6} S cm^{-1}). To further study the electrical conductivity of **Ni-COF**, a thin film was prepared on a quartz substrate and its electrical conductivity was measured by the van der Pauw method.[33] The electrical conductivity of **Ni-COF** increases linearly with temperature, which shows a high electrical conductivity of 1.2 S cm^{-1} at room temperature with a semiconducting nature (Fig. 2i). The electric conductivity of **Ni-COF** is superior to that of most of the reported COFs and COF composites, such as PEDOT@AQ-COF (1.1 S cm^{-1}),[14] TThPP films (2.38×10^{-6} S cm^{-1}),[16] ICOFs (7.2×10^{-3} S cm^{-1}),[17] PyVg-COF (4×10^{-3} S cm^{-1}),[18] Li^+@TPB-BMTP-COF (5.49×10^{-4} S cm^{-1})[19] and TpPa-SO_3Li (2.7×10^{-5} S cm^{-1}).[20] The high electrical conductivity can be attributed to the strong π-conjugation and square-planar Ni(II) coordination.

The capacitive properties of the 2D conductive **Ni-COF** were firstly evaluated in a three-electrode system in 3 M KOH. The cyclic voltammetry (CV) curves of the **Ni-COF** electrode at different scan rates in the potential range of 0–0.6 V *vs.* Hg/HgO are presented in Fig. 3a. The CV curves demonstrate a pair of strong redox peaks, indicating that the energy storage and conversion are dominated by redox reactions. The shape of the CV curves is well maintained as the scan rate increased from 5 to 30 mV s^{-1}, indicating fast charge transfer kinetics. Fig. 3b presents the galvanostatic charge/discharge (GCD) curves of the **Ni-COF** electrode at various current densities. The arch GCD profiles are in agreement with the CV analysis that **Ni-COF** is pseudo-capacitive. The capacitances were calculated to be 1478, 1257, 1054, 928, 860 and 711 F g^{-1} at 0.5, 1, 2, 3, 5 and 10 A g^{-1}, respectively (Fig. S17 and 3c†). To preclude the impact of the Ni foam substrate on the capacitance, its electrochemical properties were evaluated (Fig. S18†). The experimental results suggested that the contribution from the Ni foam substrate (48 F g^{-1}) to the total capacity is negligible. The capacitances of **Ni-COF** at 0.5 and 1 A g^{-1} are much higher than those of **Ni_0-COF** (204 and 184 F g^{-1}, respectively), again confirming the importance of the square-planar Ni(II) coordination (Fig. 3c and d, S19, S20†). The capacitance of **Ni-COF** is superior to that of previously reported COF electrode materials, DAAQ-TFP COF (49 F g^{-1} at 0.1 A g^{-1}),[34] $[TEMPO]_{100\%}$-NiP-COF (167 F g^{-1} at 0.1 A g^{-1}),[35] DqTp-COF (154 F g^{-1} at 1.56 mA cm^{-2}),[36] TpOMe-DAQ (169 F g^{-1} at 3.3 mA cm^{-2}),[37] PEDOT-modified DAAQ-TFP-COF (197 F g^{-1} at 20 mV s^{-1}),[15] TaPa-Py-COF (209 F g^{-1} at 0.5 A g^{-1}),[38] TpPa-$(OH)_2$ (416 F g^{-1} at 0.5 A g^{-1}),[39] and TDFP-1 (418 F g^{-1} at 0.5 A g^{-1}).[40] The specific capacitance of **Ni-COF** is also comparable to that of COF composites and high-performance MOFs, such as PEDOT@AQ-COF (1663 F g^{-1} at 1 A g^{-1})[14] and Co-LMOF (2474 F g^{-1} at 1 A g^{-1}).[41]

The stability test of the **Ni-COF** electrode was performed at 1 A g^{-1}. It demonstrates high stability with a high capacitance retention of 94% after 10 000 cycles (Fig. 3e). Electrochemical impedance spectroscopy (EIS) tests were carried out. According to the Nyquist plots (Fig. 3f), the **Ni-COF** electrode displays lower charge transfer resistance (R_{ct}) and equivalent series

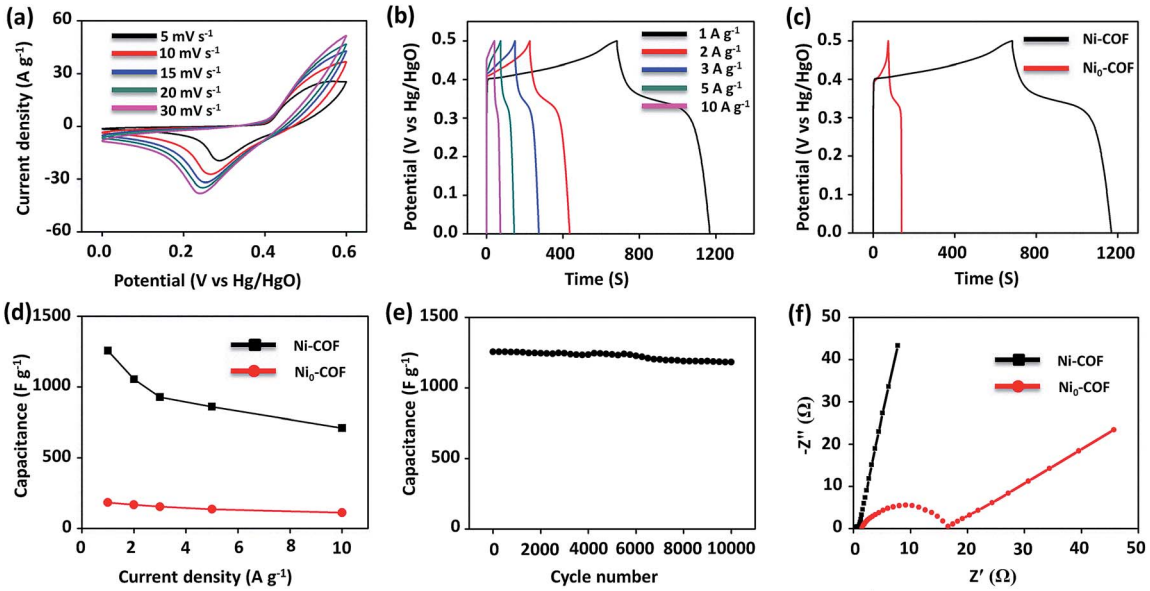

Fig. 3 Electrochemical properties of **Ni-COF** in a three-electrode system. (a) CV curves at scan rates from 5 to 30 mV s^{-1}. (b) GCD curves at different current densities (1–10 A g^{-1}). (c) Comparison of GCD curves at 1 A g^{-1} for **Ni-COF** and **Ni_0-COF**. (d) Capacitance *vs.* current density for **Ni-COF** and **Ni_0-COF**. (e) Cycling stability measurement at a current density of 1 A g^{-1}. (f) Comparison of Nyquist plots of **Ni-COF** and **Ni_0-COF**.

resistance (R_s) than **Ni_0-COF**. R_{ct} and R_s are indicated by the diameter of the semicircle and the *X*-intercept of the Nyquist plot. This confirms the high electrical conductivity of **Ni-COF**. The slope of the linear part of the Nyquist plot of **Ni-COF** is larger than that of **Ni_0-COF**, indicative of faster ion transport at the electrolyte/**Ni-COF** interfaces.

To evaluate the practical electrochemical performance, an asymmetric supercapacitor was made with activated carbon (AC) and **Ni-COF.** As shown by the CV curves in Fig. 4a and GCD profiles in Fig. 4b, the working potential window of the AC//**Ni-COF** supercapacitor can reach as large as 1.5 V. The rate capability of the AC//**Ni-COF** supercapacitor was firstly evaluated using CV measurements by varying the scan rate (Fig. 4c). The well-maintained shape of the CV curves suggests its good rate capability. Then GCD measurements were carried out at varied current densities from 1 to 10 A g^{-1} (Fig. 4d). The specific

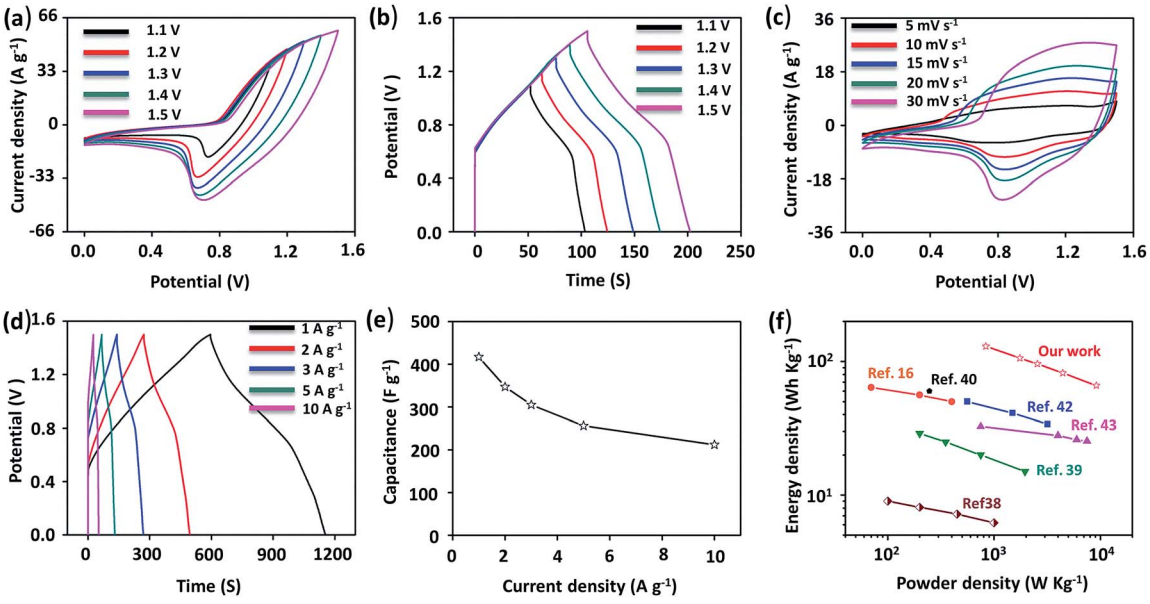

Fig. 4 Electrochemical properties of the AC//**Ni-COF** supercapacitor. (a) CV profiles of the device at a scan rate of 100 mV s^{-1} in different potential windows. (b) The GCD profiles of the device measured at a current density of 4 A g^{-1} in different potential windows. (c) CV curves with scan rates from 5 to 30 mV s^{-1}. (d) GCD profiles at different current densities (1–10 A g^{-1}). (e) The specific capacitance at different current densities (1–10 A g^{-1}). (f) Energy density of **Ni-COF**.

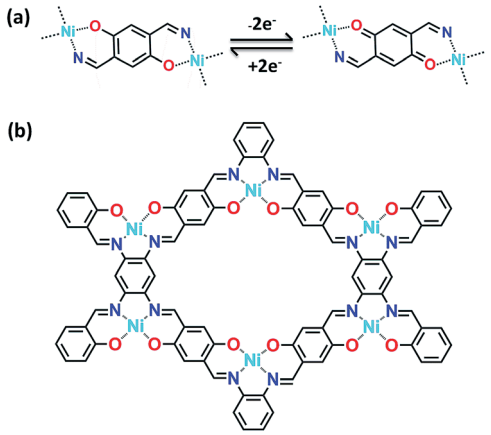

Scheme 1 Illustration of the energy storage/conversion mechanism of Ni-COF. (a) Redox reaction. (b) π-conjugated structure.

capacitances were calculated to be 417, 347, 305, 256 and 212 F g^{-1} at 1, 2, 3, 5, and 10 A g^{-1}, respectively. The capacitance at 10 A g^{-1} reached 50% of the value at 1 A g^{-1}, confirming its good rate performance (Fig. 4e). The energy density and power density of the AC//**Ni-COF** supercapacitor were presented in a Ragone plot (Fig. 4f). The energy density reaches 130 W h kg^{-1} at a power density of 839 W kg^{-1}, which outperforms that of previously reported COF-based electrode materials and is also comparable to that of MOF-based electrode materials, such as TThPP (62.44 W h kg^{-1} at 70.04 W kg^{-1}),[16] TaPa-Py-COF (9.06 W h kg^{-1} at 100 W kg^{-1}),[38] TpPa-$(OH)_2$ (29 W h kg^{-1} at 1956 W kg^{-1}),[39] TDFP-1 (58 W h kg^{-1} at 247 W kg^{-1}),[40] NiCo-MOF (49.4 W h kg^{-1} at 562.5 W h kg^{-1})[42] and GM-LEG@Ni-MOF (32.7 W h kg^{-1} at 750 W kg^{-1}).[43]

The possible energy storage/conversion mechanism is proposed in Scheme 1. Upon charging, hydroquinone is transformed into benzoquinone, which results in two-electron transfer (Scheme 1a).[44] The presence of Ni(II) favours the hydroquinone to benzoquinone transformation. Coupled with the 2D highly conjugated planar structure, the high electrical conductivity of **Ni-COF** helps the electron transport throughout each 2D planar layer (Scheme 1b).

In summary, by incorporating Ni^{2+} into COF frameworks, a 2D highly conjugated semiconducting **Ni-COF** has been synthesized as an advanced electrode material for supercapacitors. **Ni-COF** shows a high specific capacitance of 1257 F g^{-1} at 1 A g^{-1}, excellent cycling stability with 94% capacitance retention after 10 000 cycles and an outstanding energy density of 130 W h kg^{-1} at a power density of 839 W kg^{-1}. The high electrochemical performance can be mainly ascribed to the highly enhanced electrical conductivity, conjugated planar structure, and high-density redox-active centres. This work paves the way to improve the energy storage capacity of functional COFs in supercapacitors.

Conflicts of interest

There are no conflicts to declare.

Acknowledgements

This work was supported by the National Natural Science Foundation of China (21771089), the Fundamental Research Funds for the Central Universities (JUSRP21936, JUSRP51725B, and JUSRP11930), the Project for Jiangsu Scientific and Technological Innovation Team, and MOE & SAFEA for the 111 Project (B13025).

References

1 G. Liu, C. Zhen, Y. Y. Kang, L. Z. Wang and H. M. Cheng, *Chem. Soc. Rev.*, 2018, **47**, 6410–6444.
2 L. L. Mao, C. C. Staumpos and M. G. Kanatzidis, *J. Am. Chem. Soc.*, 2019, **141**, 1171–1190.
3 Y. W. Liu, C. Xiao, P. C. Huang, M. Cheng and Y. Xie, *Chem*, 2018, **4**, 1263–1283.
4 Y. X. Chen, K. N. Yang, B. Jiang, J. X. Li, M. Q. Zeng and L. Fu, *J. Mater. Chem. A*, 2017, **5**, 8187–8208.
5 Q. B. Yun, Q. P. Lu, X. Zhang, C. L. Tan and H. Zhang, *Angew. Chem., Int. Ed.*, 2018, **57**, 626–646.
6 G. Zhang, H. J. Liu, J. H. Qu and J. H. Li, *Energy Environ. Sci.*, 2016, **9**, 1190–1209.
7 G. X. Zhang, X. Xiao, B. Li, P. Gu, H. G. Xue and H. Pang, *J. Mater. Chem. A*, 2017, **5**, 8155–8186.
8 V. M. H. Ng, H. Huang, K. Zhou, P. S. Lee, W. X. Que, J. Z. C. Xu and L. B. Kong, *J. Mater. Chem. A*, 2017, **5**, 3039–3068.
9 J. Yang, P. X. Xiong, C. Zheng, H. Y. Qiu and M. D. Wei, *J. Mater. Chem. A*, 2014, **2**, 16640–16644.
10 F. X. Wang, X. W. Wu, X. H. Yuan, Z. C. Liu, Y. Zhang, L. J. Fu, Y. S. Zhu, Q. M. Zhou, Y. P. Wu and W. Huang, *Chem. Soc. Rev.*, 2017, **46**, 6816–6854.
11 P. F. Wei, M. Z. Qi, Z. P. Wang, S. Y. Ding, W. Yu, Q. Liu, L. K. Wang, H. Z. Wang, W. K. An and W. Wang, *J. Am. Chem. Soc.*, 2018, **140**, 4623–4631.
12 F. Beuerle and B. Gole, *Angew. Chem., Int. Ed.*, 2018, **57**, 4850–4878.
13 Y. Yan, P. Gu, S. S. Zheng, M. B. Zheng, H. Pang and H. G. Xue, *J. Mater. Chem. A*, 2016, **4**, 19078–19085.
14 Y. Wu, D. W. Yan, Z. Y. Zhang, M. M. Matsushita and K. Awaga, *ACS Appl. Mater. Interfaces*, 2019, **11**, 7661–7665.
15 C. R. Mulzer, L. X. Shen, R. P. Bisbey, J. R. McKone, N. Zhang, H. D. Abruña and W. R. Dichtel, *ACS Cent. Sci.*, 2016, **2**, 667–673.
16 H. Yang, S. L. Zhang, L. H. Han, Z. Zhang, Z. Xue, J. Gao, Y. J. Li, C. S. Huang, Y. P. Yi, H. B. Liu and Y. L. Li, *ACS Appl. Mater. Interfaces*, 2016, **8**, 5366–5375.
17 Y. M. Hu, N. Dunlap, S. Wan, S. L. Lu, S. F. Huang, I. Sellinger, M. Ortiz, Y. H. Jin, S. H. Lee and W. Zhang, *J. Am. Chem. Soc.*, 2019, **141**, 7518–7525.
18 L. L. Wang, C. Zeng, H. Xu, P. C. Yin, D. C. Chen, J. Deng, M. Li, N. Zheng, C. Gu and Y. G. Ma, *Chem. Sci.*, 2019, **10**, 1023–1028.
19 Q. Xu, S. S. Tao, Q. H. Jiang and D. L. Jiang, *J. Am. Chem. Soc.*, 2018, **140**, 7429–7432.

20 K. Jeong, S. Park, G. Y. Jung, S. H. Kim, Y. H. Lee, S. K. Kwak and S. Y. Lee, *J. Am. Chem. Soc.*, 2019, **141**, 5880–5885.
21 D. W. Feng, T. Lei, M. R. Lukatskaya, J. Park, Z. H. Huang, M. Lee, L. Shaw, S. C. Chen, A. A. Yakovenko, A. Kulkarni, J. P. Xiao, K. Fredrickson, J. B. Tok, X. D. Zou, Y. Cui and Z. N. Bao, *Nat. Energy*, 2018, **3**, 30.
22 D. Sheberla, J. C. Bachman, J. S. Elias, C. J. Sun, Y. S. Horn and M. Dinca, *Nat. Mater.*, 2017, **16**, 220.
23 D. A. Vazquez-Molina, G. S. Mohammad-Pour, C. Lee, M. W. Logan, X. F. Duan, J. K. Harper and F. J. Uribe-Romo, *J. Am. Chem. Soc.*, 2016, **138**, 9767–9770.
24 B. P. Biswal, S. Chandra, S. Kandambeth, B. Lukose, T. Heine and R. Banerjee, *J. Am. Chem. Soc.*, 2013, **135**, 5328–5331.
25 G. Q. Lin, H. M. Ding, R. F. Chen, Z. K. Peng, B. S. Wang and C. Wang, *J. Am. Chem. Soc.*, 2017, **139**, 8705–8709.
26 H. Wei, S. Z. Chai, N. T. Hu, Z. Yang, L. M. Wei and L. Wang, *Chem. Commun.*, 2015, **51**, 12178–12181.
27 X. Han, Q. C. Xia, J. J. Huang, Y. Liu, C. X. Tan and Y. Cui, *J. Am. Chem. Soc.*, 2017, **139**, 8693–8697.
28 L. H. Li, X. L. Feng, X. H. Cui, Y. X. Ma, S. Y. Ding and W. Wang, *J. Am. Chem. Soc.*, 2017, **139**, 6042–6045.
29 Y. Z. Liao, H. G. Wang, M. F. Zhu and A. Thomas, *Adv. Mater.*, 2018, **30**, 1705710.
30 F. L. Li, Q. Shao, X. Q. Huang and J. P. Lang, *Angew. Chem., Int. Ed.*, 2018, **57**, 1888–1892.
31 J. Jin, Y. Zheng, S. Z. Huang, P. P. Sun, N. Srikanth, L. B. Kong, Q. Y. Yan and K. Zhou, *J. Mater. Chem. A*, 2019, **7**, 783–790.
32 S. Dalapati, E. Jin, M. Addicoat, T. Heine and D. L. Jiang, *J. Am. Chem. Soc.*, 2016, **138**, 5797–5800.
33 D. Sheberla, L. Sun, M. A. Blood-Forsythe, S. Er, C. R. Wade, C. K. Brozek, A. Aspuru-Guzik and M. Dincă, *J. Am. Chem. Soc.*, 2014, **136**, 8859–8862.
34 C. R. DeBlase, K. E. Silberstein, T. T. Truong, H. D. Abruña and W. R. Dichtel, *J. Am. Chem. Soc.*, 2013, **135**, 16821–16824.
35 F. Xu, H. Xu, X. Chen, D. C. Wu, Y. Wu, H. Liu, C. Gu, R. W. Fu and D. L. Jiang, *Angew. Chem., Int. Ed.*, 2015, **54**, 6814–6818.
36 M. A. Khayum, V. Vijayakumar, S. Karak, S. Kandabeth, M. Bhadra, K. Suresh, N. Acharambath, S. Kurungot and R. Banerjee, *ACS Appl. Mater. Interfaces*, 2018, **10**, 28139–28146.
37 A. Halder, M. Ghosh, M. A. Khayum, S. Bera, M. Addicoat, H. S. Sasmal, S. Karak, S. Kurungot and R. Banerhee, *J. Am. Chem. Soc.*, 2018, **140**, 10941–10945.
38 A. M. Khattak, Z. A. Ghazi, B. Liang, N. A. Khan, A. Iqbal, L. S. Li and Z. Y. Tang, *J. Mater. Chem. A*, 2016, **4**, 16312–16317.
39 S. Chandra, D. R. Chowdhury, M. Addicoat, T. Heine, A. Paul and R. Banerjee, *Chem. Mater.*, 2017, **29**, 2074–2080.
40 P. Bhanja, K. Bhunia, S. K. Das, D. Pradhan, R. Kimura, Y. Hijikata, S. Irle and A. Bhaumik, *ChemSusChem*, 2017, **10**, 921–929.
41 X. X. Liu, C. D. Shi, C. W. Zhai, M. L. Cheng, Q. Liu and G. X. Wang, *ACS Appl. Mater. Interfaces*, 2016, **8**, 4585–4591.
42 Y. Z. Wang, Y. X. Liu, H. Q. Wang, W. Liu, Y. Li, J. F. Zhang, H. Hou and J. L. Yang, *ACS Appl. Energy Mater.*, 2019, **2**, 2063–2071.
43 Y. Xiao, W. Wei, M. J. Zhang, S. Jiao, Y. C. Shi and S. J. Ding, *ACS Appl. Energy Mater.*, 2019, **2**, 2169–2177.
44 Z. R. Lou, P. Li and K. L. Han, *Acc. Chem. Res.*, 2015, **48**, 1358–1368.

Supporting Information for

A two-dimensional semiconducting covalent organic framework with nickel(II) coordination for high capacitive performance

Tao Li,[a] Wen-Da Zhang,[a] Yong Liu,[a] Yunxing Li,[a] Caikun Cheng,[a] Haiyan Zhu,[a] Xiaodong Yan,[a] Zaijun Li,*[a] and Zhi-Guo Gu*[ab]*

[a] *Key Laboratory of Synthetic and Biological Colloids, Ministry of Education, School of Chemical and Material Engineering, Jiangnan University, Wuxi 214122, China*

[b] *International Joint Research Center for Photoresponsive Molecules and Materials, School of Chemical and Material Engineering, Jiangnan University, Wuxi 214122, China*

E-mail: zhiguogu@jiangnan.edu.cn

1. General Information

All reagents and solvents were reagent grade, purchased from commercial sources and used without further purification. Fourier transform infrared (FT-IR) spectra were performed on a Thermo Nicolet iS10 spectrometer in the spectral range of 500-4000 cm^{-1}. ^{13}C cross-polarization with magic angle-spinning (CP-MAS) solid-state nuclear magnetic resonance (NMR) spectra were recorded on a Bruker ARX 300 MHz spectrometer. Mass spectra (MS) were taken on a Waters MALDI SYNAPT G2 Series spectrometer. X-ray photoelectron spectroscopy (XPS) analysis was measured by a Kratos Axis Supra instrument (Kratos Analytical, Manchester, UK) using a monochromatized Al Ka radiation as X-ray source. Thermogravimetric analyses (TGA) were obtained using a Mettler Toledo TGA/DSC1/1100SF analyser in the temperature range of 30 to 800 °C under flowing N_2. The Brunauer-Emmett-Teller (BET) surface areas were observed on N_2 sorption isotherms at 77 K using a Micromeritics ASAP2020 surface area and pore size analyser. Pore size distribution was determined by nonlocal density functional theory mode in the instrument software package. Scanning electron microscopy (SEM) images were obtained on a Hitachi S-4800. Transmission electron microscopy (TEM) images were observed on a JEOL JEM-2100. Scanning transmission electron microscopy (STEM) images, HRTEM images and EDS mapping were carried out on a Tecnai G2 F30 transmission electron microscopy at an acceleration voltage of 300 kV. Powder electrical conductivity was recorded on a Suzhou Jingge ST2253 by four-probe method. Thin film electrical conductivity was measured by the van der Pauw method under temperature control, the date was collected using a Keithley 4200-SCS parameter analyzer.

2. Electrochemical performance experiments

The electrochemical performances of the samples were carried out on an electrochemical station (CHI660E). Cyclic voltammetry (CV), galvanostatic charge-discharge (GCD) and Electrochemical impedance spectroscopy (EIS) measurement were conducted on in a three-electrode setup, including a Pt plate (1 cm^2) as the counter electrode and Hg/HgO electrode as the reference electrode. The working electrode was prepared by mixing active material, acetylene black and poly(tetrafluoethylene) in a mass ratio of 8:1:1, and then dispersed in ethanol by ultrasonication to obtain homogeneous slurry. The slurry was coated on a Ni foam substrate (1 cm^2). The mass loading of active materials on Ni foam was 5.0 mg cm^{-2}. Moreover, the asymmetric supercapacitor devices were assembled to test the electrochemical performance, with activated materials acting as the positive, activated carbon (AC) as the negative electrode. All the electrochemical measurements were recorded on using 3 M KOH aqueous electrolyte. EIS measurements were collected in the frequency range from 0.01 to 10^5 Hz at open circuit potential with a sinus amplitude of 5 mV.

3. Calculation Section

The specific capacitance of electrode materials was calculated by the following equation (1) and equation (2):[1]

$$E_{\text{int}/D} = I \int_{t(U_{\min})}^{t(U_{\max})} U(t)dt \quad (1)$$

$$C_{\text{int}/D} = \frac{2E_{\text{int}/D}}{U_{\max}^2} \quad (2)$$

Where $E_{int/D}$ is the energy density (Wh kg^{-1}), I is the discharge current, U is the potential range (V), t is the discharge time (s), $C_{int/D}$ is the specific capacitance (F g^{-1}). Energy density and power density of the **PG-BBT** are evaluated according to equation (3) and equation (4), respectively:

$$E = \frac{1}{2} C_{sp} V^2 \quad (3)$$

$$P = \frac{E}{\Delta t} \quad (4)$$

where E stands for the energy density (Wh kg^{-1}), C_{sp} represents the specific capacitance (F g^{-1}), V refers to the potential window (V), P is the power density (W kg^{-1}) and Δt is the discharge time (S).

4. Experimental section

Synthesis of Ni-COF

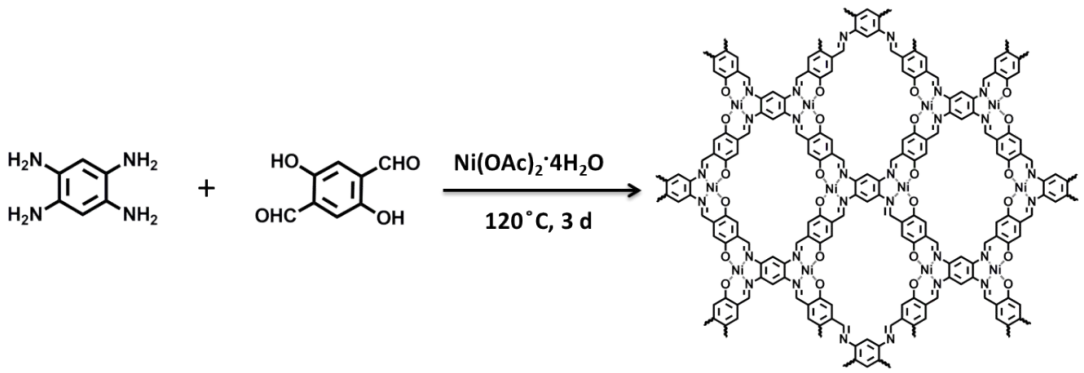

A glass bottle (volume of ca. 10 mL) was charged with 1,2,4,5-benzenetetraamine tetrahydrochloride (BTA) (20 mg, 0.07 mmol), 2,5-dihydroxy-1,4-benzenedicarboxaldehyde (HBC) (27.4 mg, 0.14 mmol), excess $Ni(OAc)_2 \cdot 4H_2O$, 0.5 mL of mesitylene and 1.5 mL of 1,4-dioxane. The resulting solution was sonicated for 10 minutes to obtain a homogenous dispersion. The glass bottle was transferred into a 25 mL Teflon-lined stainless steel autoclave. The autoclave was sealed and heated at 120 °C for 3 days and cooled to room temperature. The formed black precipitate was collected by filtration and washed with THF (3 × 20 mL), DMF (3 × 20 mL) and MeOH (3 × 20 mL), Soxhlet extracted by THF 24 h, then dried at 80 °C under vacuum for 24 h to give a black powder with 86% yield. FT-IR (powder): ν_{max} 3281, 2566, 1621, 1563, 1508, 1435, 1372, 1295, 1227, 1127, 1056, 1001, 866, 801, 676, 612 and 558 cm^{-1}.

Synthesis of Ni_0-COF

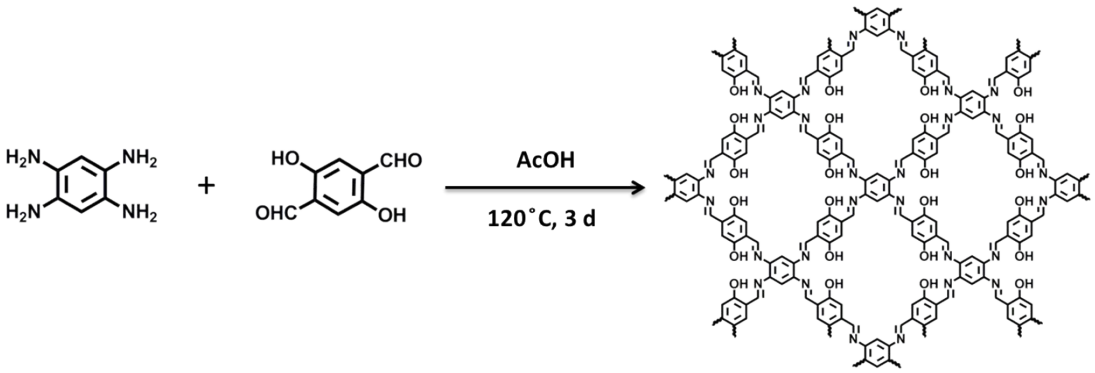

A glass bottle (volume of ca. 10 mL) was charged with 1,2,4,5-benzenetetraamine tetrahydrochloride (BTA) (20 mg, 0.07 mmol), 2,5-dihydroxy-1,4-benzenedicarboxaldehyde (HBC) (27.4 mg, 0.14 mmol), 0.5 mL of mesitylene and 1.5 mL of 1,4-dioxane. The resulting solution was sonicated for 10 minutes to obtain a homogenous dispersion, and then added 0.2 mL of 3 M aqueous acetic acid (AcOH). The glass bottle was transferred into a 25 mL Teflon-lined stainless steel autoclave. The autoclave was sealed and heated at 120 °C for 3 days and cooled to room temperature. The formed brown precipitate was collected by filtration and washed with THF (3 × 20 mL), DMF (3 × 20 mL) and MeOH (3 × 20 mL), Soxhlet extracted by THF 24 h, then dried at 80 °C under vacuum for 24 h to give a black powder with 81% yield. FT-IR (powder): ν_{max} 3072, 1621, 1576, 1492, 1431, 1358, 1281, 1258, 1202, 1157, 968, 857, 797, 743, 670 and 617 cm^{-1}.

5. Characterization

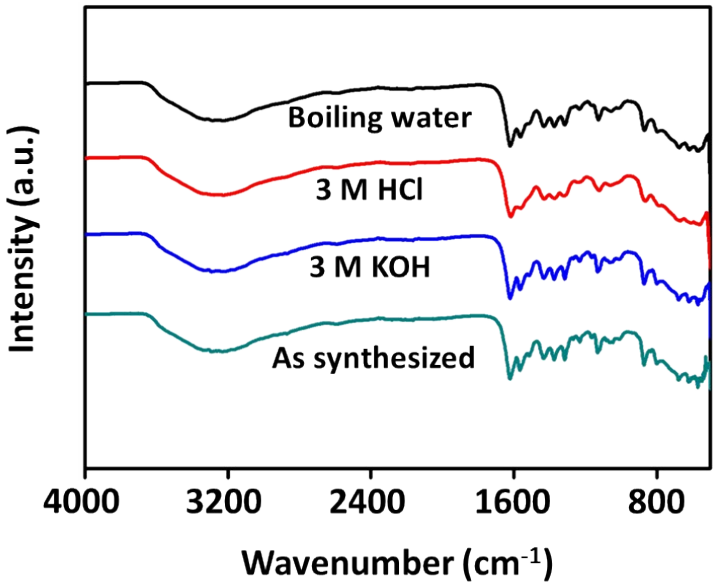

Fig. S1 Chemical stability tests of **Ni-COF**. The FT-IR patterns of **Ni-COF** treated for 5 days in different solvents.

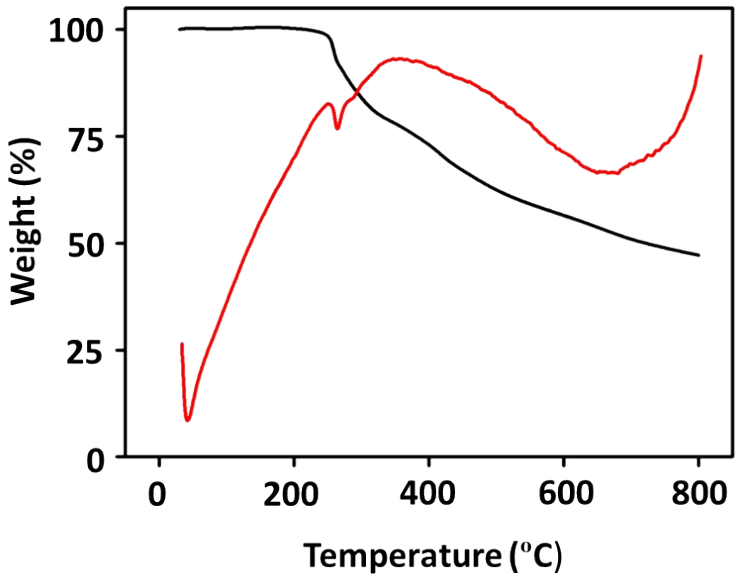

Fig. S2 Thermogravimetric analysis (TGA) curve of **Ni-COF**.

Ni-COF exhibited no discernible weight loss from 0 to 253 °C, and then **Ni-COF** started to decompose. At 800 °C, there was still 53% of weight residual for **Ni-COF**, indicating its excellent thermal stability.

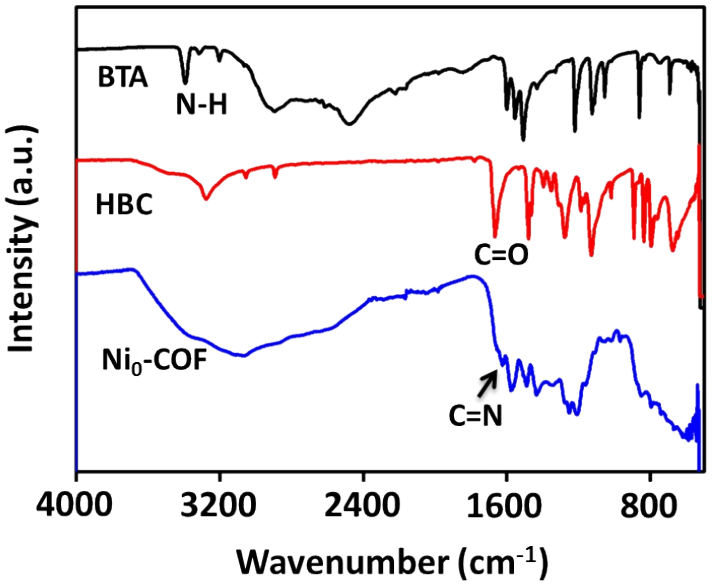

Fig. S3 FT-IR spectra of BTA, HBC and **Ni_0-COF**.

The disappearance of the characteristic C=O vibration band (1654 cm^{-1}), N-H vibration band (3389-3197cm^{-1}), and the appearance of C=N bonding (1621 cm^{-1}), indicates the formation of **Ni_0-COF**.

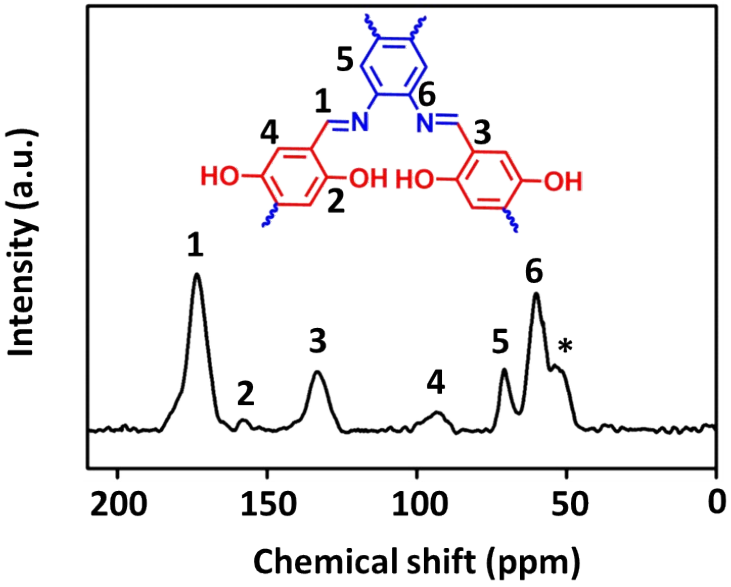

Fig. S4 Solid-state ^{13}C NMR spectrum of **Ni_0-COF**.

The characteristic resonance signal at 173 and 156 ppm is assigned to the C=N and C-O groups, respectively, which clearly reveals the formation of **Ni_0-COF**.

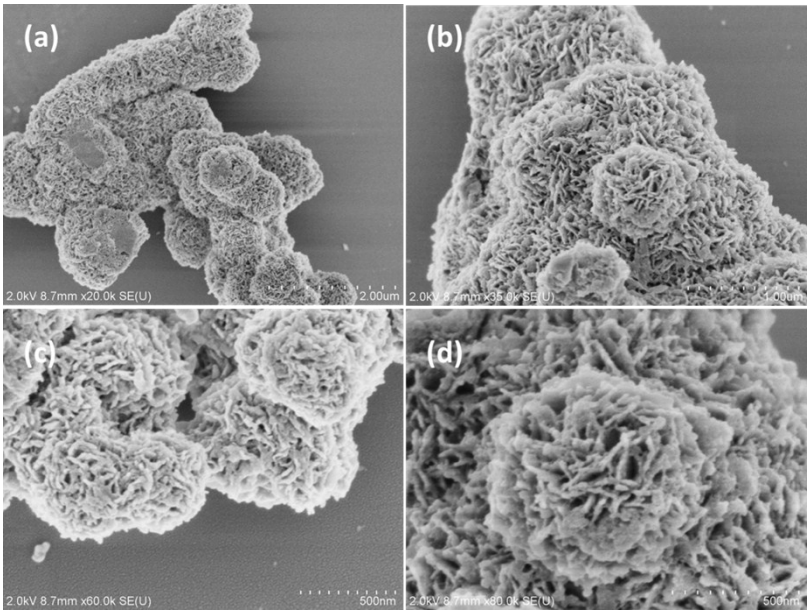

Fig. S5 SEM of **Ni-COF**.

The SEM images of **Ni-COF** show a spherical flower-like morphology, which is composed of numerous sheets.

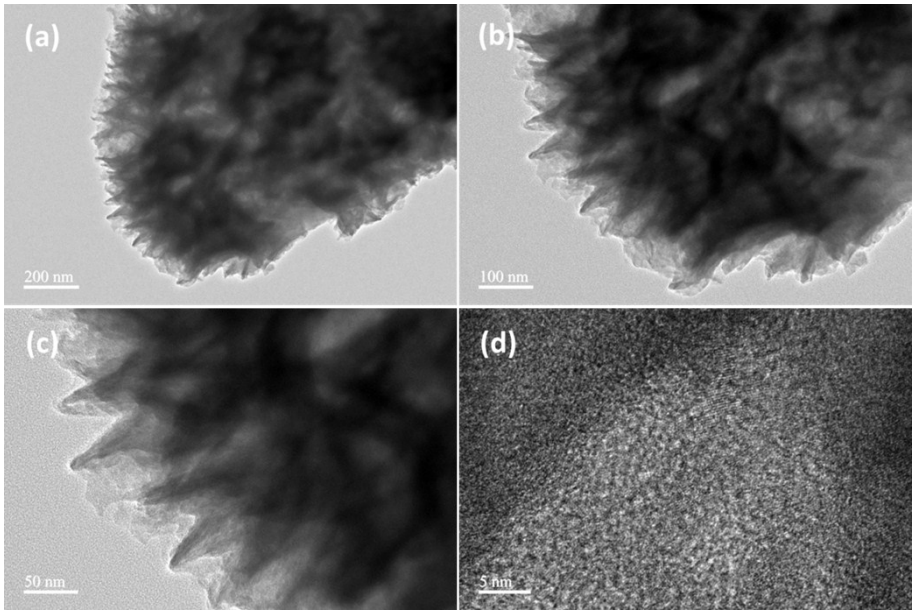

Fig. S6 TEM of **Ni-COF**.

TEM images clearly clarify that **Ni-COF** shows optically translucent feature owing to thick layer structure.

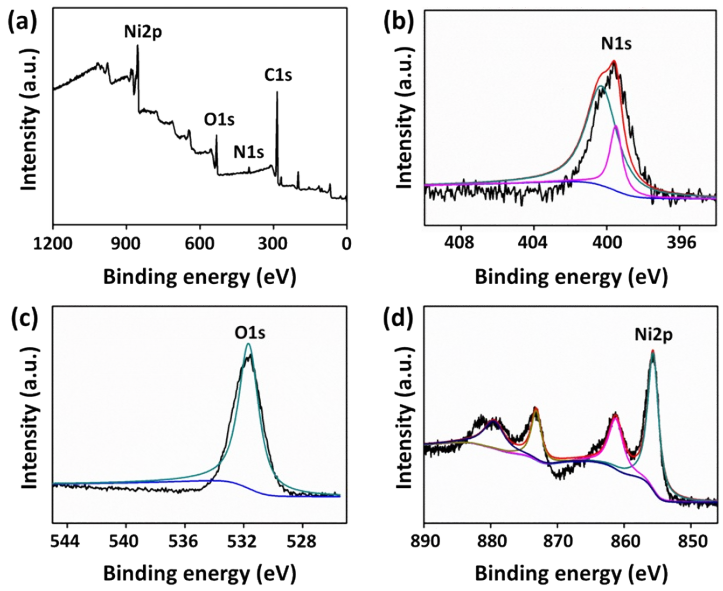

Fig. S7 XPS measurements of **Ni-COF**: (a) survey, (b) N 1s, (c) O 1s and (d) Ni 2p spectrum.

The XPS survey of Ni-COF confirms the presence of C, N, O and Ni. The signals at 399 and 532 eV correspond to N 1s and O 1s, respectively. The Ni 2p spectrum exhibits two main peaks around 856.1 and 873.6 eV that are assigned to Ni $2p_{3/2}$ and Ni $2p_{1/2}$, respectively, together with their corresponding satellite peaks around 861.3 and 880.1 eV.

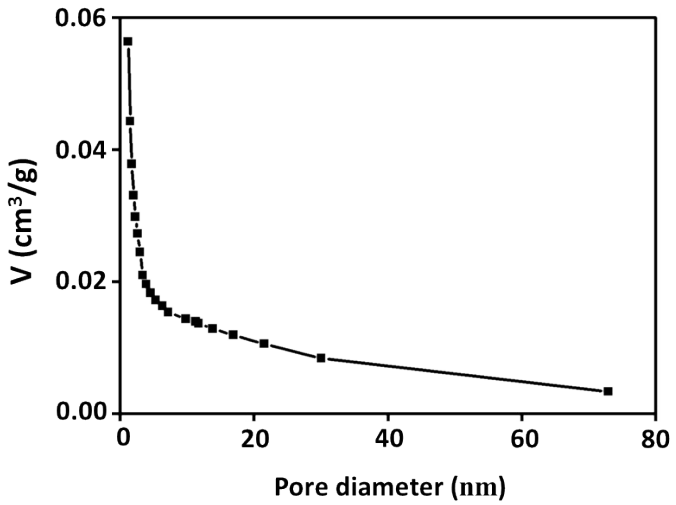

Fig. S8 Pore volume plot of **Ni-COF**.

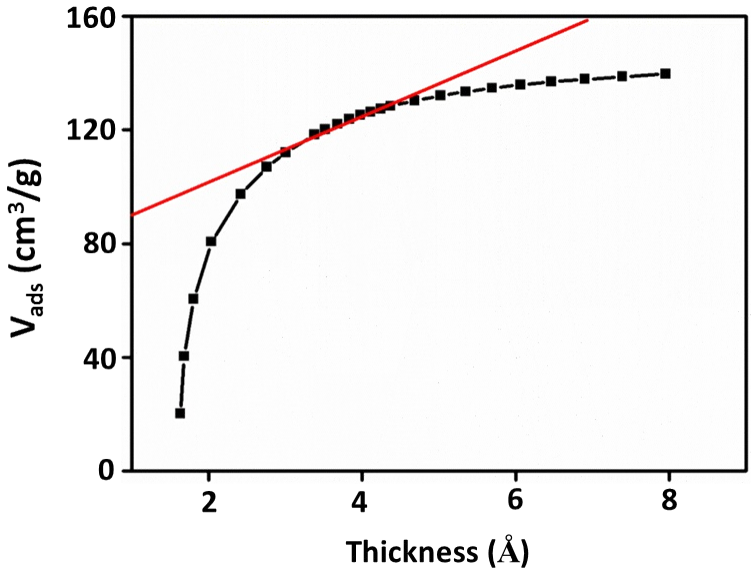

Fig. S9 t-Plots of **Ni-COF** using the Harkins and Jura reference isotherm. The lines represent the fit to the linear region, which is marked by the red symbols.

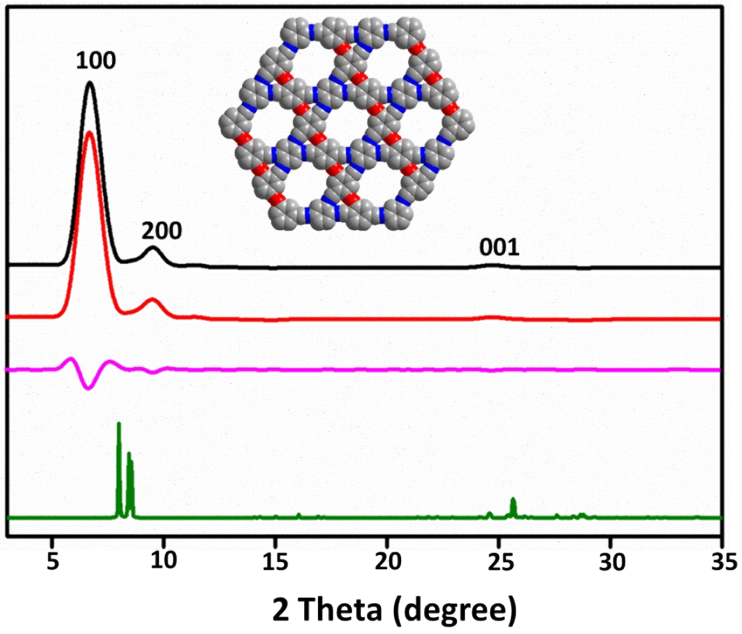

Fig. S10 PXRD patterns of **Ni_0-COF** with the experimental PXRD profiles in black, Pawley-refined profiles in red, calculated profiles in green, and the differences between the experimental and refined PXRD patterns in pink.

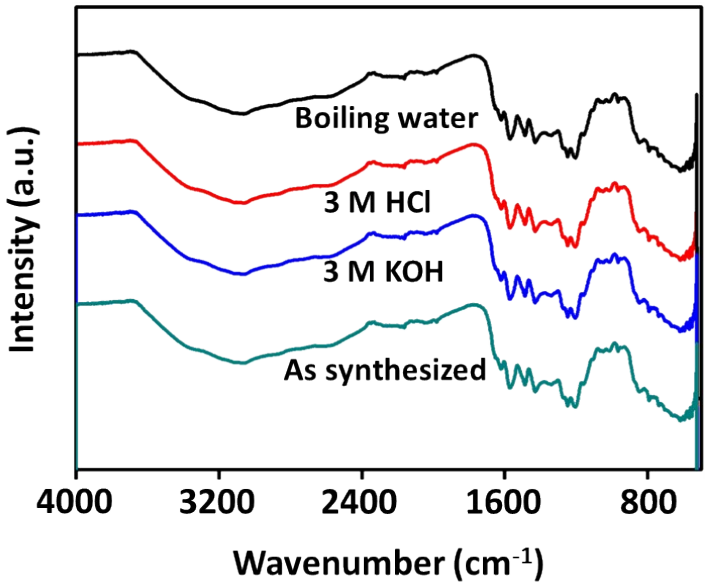

Fig. S11 Chemical stability tests of **Ni_0-COF**. The FT-IR patterns of **Ni_0-COF** treated for 5 days in different solvents.

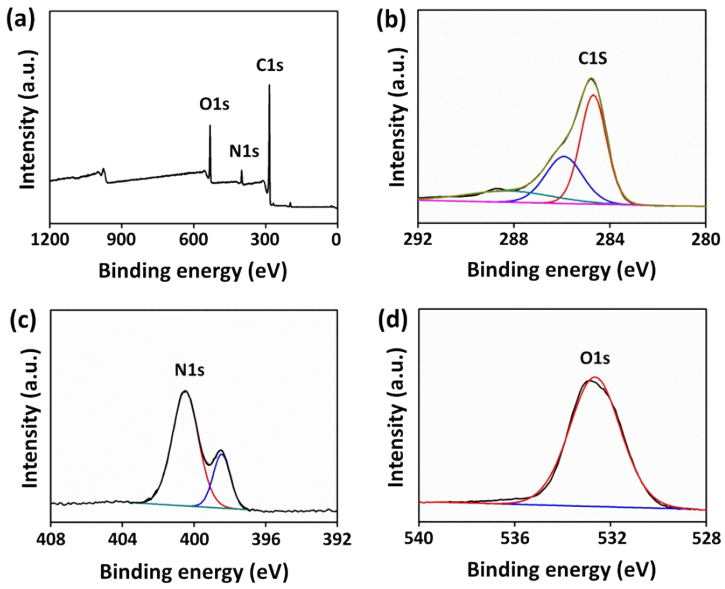

Fig. S12 XPS measurements of **Ni_0-COF**: (a) survey, (b) C1s, (c) N 1s and (d) O 1s spectra.

The XPS survey of **Ni_0-COF** confirms the presence of C, N and O. The signals at 284.8, 400.4 and 532.9 eV correspond to C1s, N 1s and O 1s, respectively.

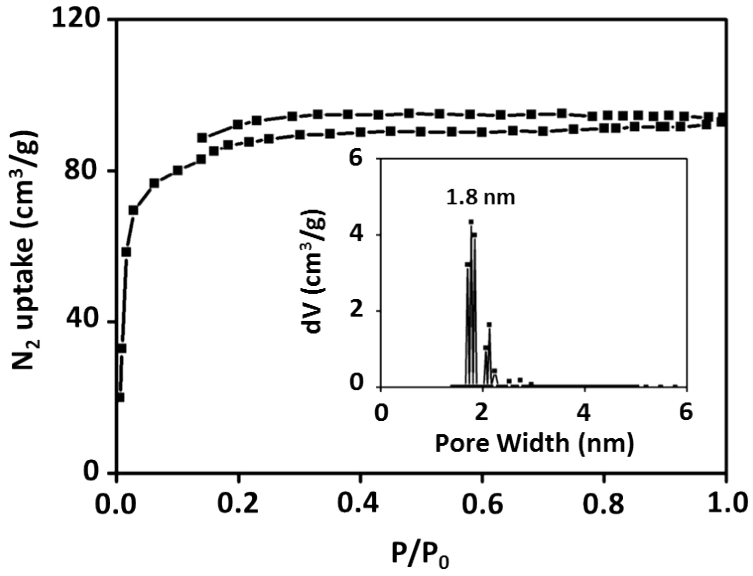

Fig. S13 Nitrogen adsorption-desorption isotherm of Ni_0-COF, and the insert exhibits the pore size distribution.

The curve displays a typical type-I shape with a sharp uptake under low relative pressure ($P/P_0 < 0.01$), indicating its microporous nature. The BET surface area of **Ni_0-COF** is estimated to be 258 $m^2 g^{-1}$. The average pore size of **Ni_0-COF** is 1.8 nm.

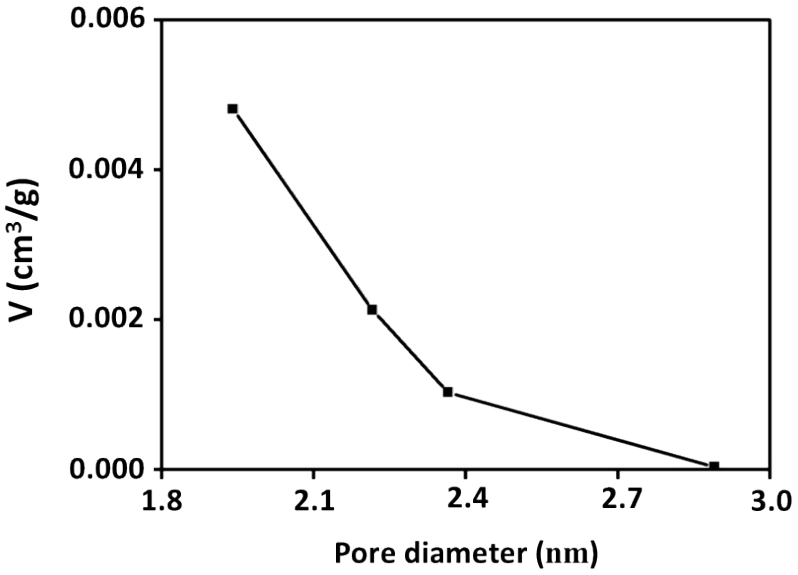

Fig. S14 Pore volume plot of **Ni_0-COF**.

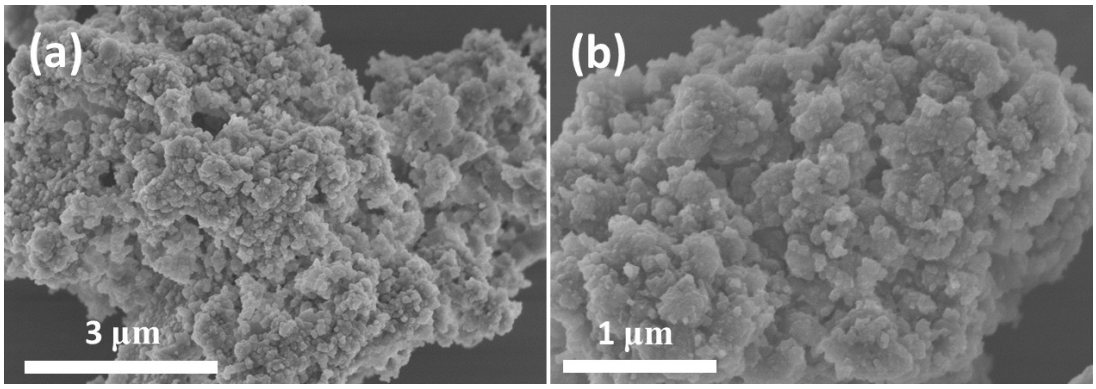

Fig. S15 SEM of **Ni_0-COF**.

The SEM images show a homogeneous morphology, which was consisted of a large number of grains.

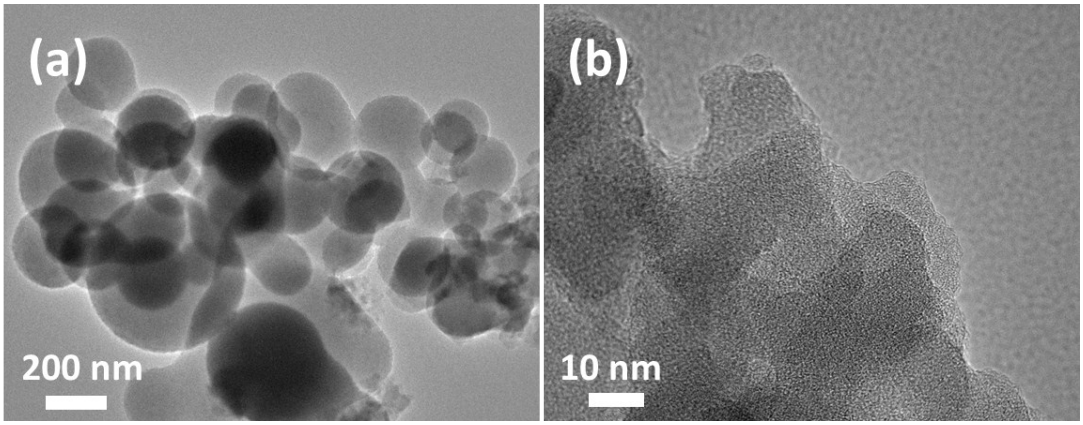

Fig. S16 TEM of **Ni_0-COF**.

The TEM images clearly observe that **Ni_0-COF** exhibits spherical grains and layer-by-layer structure.

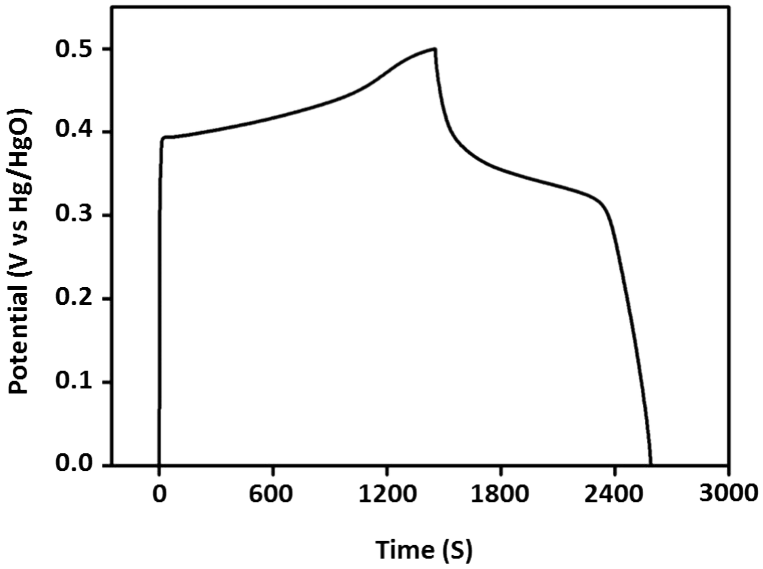

Fig. S17 GCD curve of **Ni-COF** at 0.5 A g^{-1}.

The specific capacitance of **Ni-COF** is calculated to be 1478 F g^{-1} at 0.5 A g^{-1}.

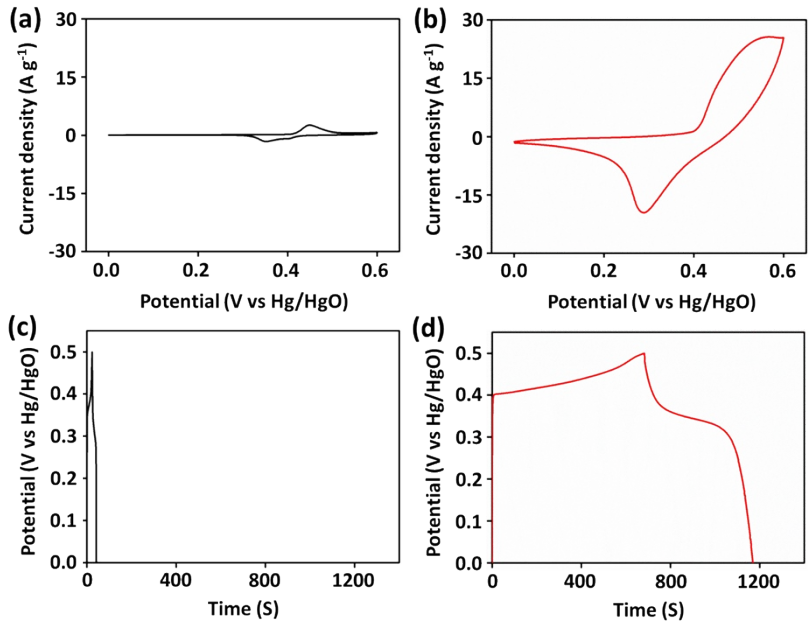

Fig. S18 CV curves of (a) Ni foam and (b) **Ni-COF** at 5 mV s^{-1}. GCD curves of (c) Ni foam and (d) **Ni-COF** at 1 A g^{-1}.

To preclude the impact of Ni foam substrate on the performance, electrochemical experiment on it was conducted (48 F g^{-1} at 1A g^{-1}). Compared with **Ni-COF** (1257 F g^{-1} at 1 A g^{-1}), the contribution from the Ni foam substrate to the total capacity is negligible.

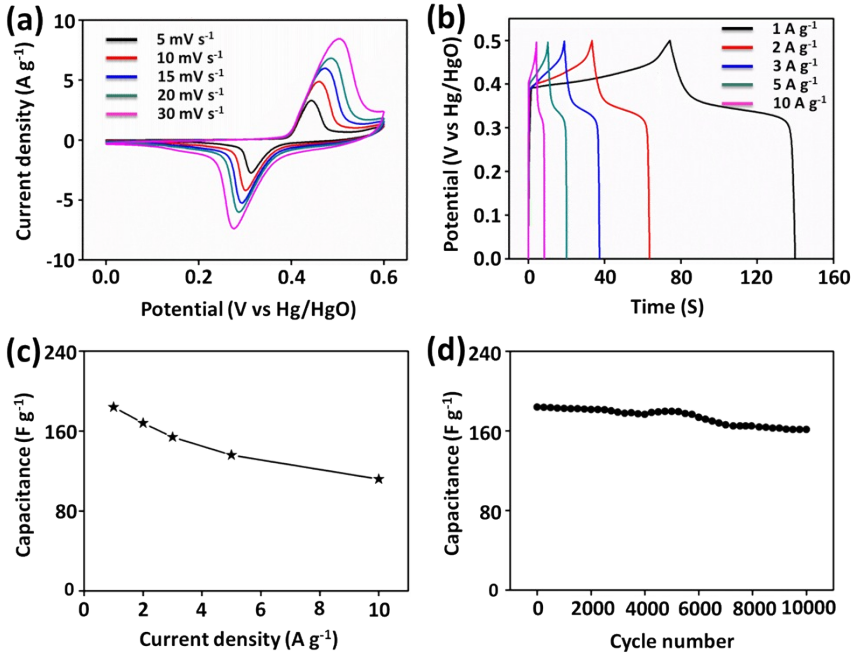

Fig. S19 Electrochemical properties of **Ni_0-COF** in a three-electrode system. (a) CV curves at scan rates from 5 to 30 mV s^{-1}. (b) GCD curves at different current densities (1-10 A g^{-1}). (c) Capacitance vs current density. (d) Cyclic stability measurement at a current density of 1 A g^{-1}.

The CV curves exhibit different scan rates from 5 to 30 mV s^{-1} and display a pair of redox peaks, indicating the pseudocapacitive behaviour. The GCD profiles show different current densities from 1 to 10 A g^{-1}. The GCD curves show a severely distorted triangular shape, which is resulted from the typical pseudocapacitive behaviour, in agreement with the CV analyses. The discharging capacitances of **Ni_0-COF** are calculated to be 184, 168, 154, 136 and 112 F g^{-1} at 1, 2, 3, 5 and 10 A g^{-1}, respectively. The specific capacitance at 10 A g^{-1} retains 61% of that at 1 A g^{-1}, indicating its good rate capability. The stability test of the **Ni_0-COF** electrode was evaluated at 1 A g^{-1}. It demonstrates high stability with high capacitance retention of 87.5 % after 10000 cycles.

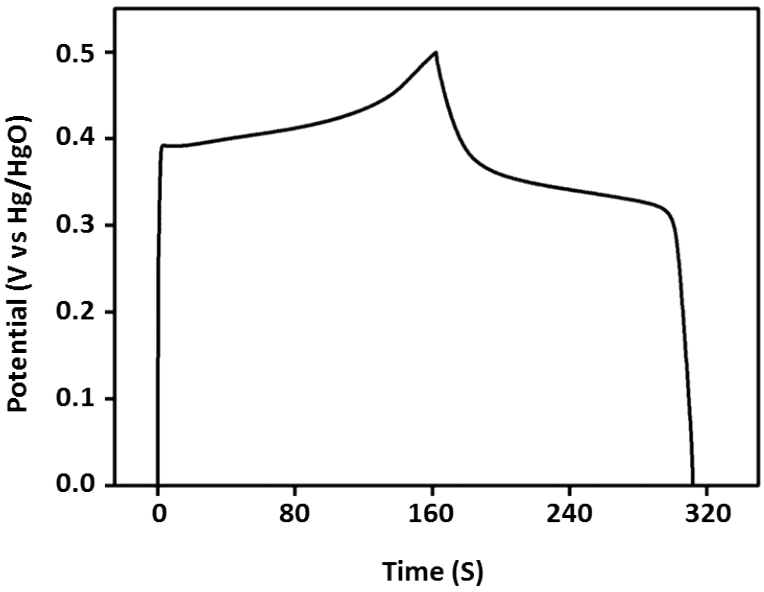

Fig. S20 GCD curve of **Ni_0-COF** at 0.5 A g^{-1}.

The specific capacitance of **Ni_0-COF** is calculated to be 204 F g^{-1} at 0.5 A g^{-1}.

Table S1. Fractional atomic coordinates for the triclinic *P*1/(1) unit cell of **Ni-COF** calculated using the Materials Studio 7.0.

Ni-COF			
Triclinic *P*1/(1) *a* = 12.8777 Å, *b* = 12.1493 Å, *c* = 14.8164 Å			
C1	1.12607	1.09325	-0.34932
C2	0.19516	1.04500	-0.28450
C3	0.08888	0.01325	0.89411
C4	-0.08759	0.01475	0.01845
C5	0.83769	0.05471	-0.03641
C6	0.95110	1.09874	-0.22850
N7	-0.19843	-0.05550	0.23180
C8	-0.30027	0.05432	1.25405
C9	-0.14787	0.28604	1.06463
C10	0.06568	0.38215	-0.10817
C11	0.19392	0.60524	0.71894
C12	0.11821	0.73890	0.70731
C13	-0.09166	0.64556	0.87511
C14	-0.22250	0.41979	1.05298
C15	0.20979	0.90225	0.61688
N16	0.18645	1.08387	0.52606
O17	0.15807	0.26699	-0.11881
O18	-0.18603	0.75377	0.89622
N19	0.18645	0.11717	-0.27905
C20	0.67973	0.05196	0.89536
C21	0.59246	0.03926	0.87628
C22	0.34446	-0.09644	0.13816

C23	0.24332	-0.12747	1.14688
C24	0.39008	-0.03002	0.89774
C25	0.64095	0.11375	0.62821
C26	0.74477	0.15176	0.61286
C27	0.26786	-0.12468	0.95940
N28	0.13234	-0.04848	0.99266
Ni29	1.08812	0.19514	0.43073
O30	-0.01515	-0.29032	0.43887
O31	1.00377	0.31728	0.31835
Ni32	1.89884	1.83119	1.32795

Table S2. Fractional atomic coordinates for the triclinic P1/(1) unit cell of **Ni_0-COF** calculated using the Materials Studio 7.0.

Ni_0-COF			
Triclinic P1/(1) *a* = 12.9144 Å, *b* = 12.4401 Å, *c* = 22.1318 Å			
C1	1.02688	0.82450	-0.08070
C2	0.09651	0.81008	-0.05189
C3	0.07812	-0.08066	0.95399
C4	-0.01143	0.06066	-0.07444
C5	0.90331	0.07226	-0.09593
C6	0.91337	0.94356	-0.09096
N7	-0.00042	0.18851	-0.09024
C8	-0.05438	0.35796	0.86442
C9	-0.02392	0.47331	0.85173
C10	0.07117	0.42719	-0.12226
C11	0.12044	0.57646	0.84158
C12	0.01958	0.71919	0.82860
C13	-0.06181	0.77289	0.79567
C14	0.08956	0.66065	0.79993
C15	0.10287	0.66450	0.86234
N16	-0.01906	0.77279	0.90680
O17	0.14064	0.27534	-0.08742
O18	-0.11796	0.92781	0.76363
N19	-0.18548	-0.06899	-0.09161
C20	0.71214	0.04998	0.88960
C21	0.58584	0.02849	0.90778
C22	0.33677	0.15746	0.91906

C23	0.28979	-0.00167	0.96692
C24	0.27058	-0.27046	1.11021
C25	0.52734	-0.12813	0.95580
C26	0.19029	-0.09786	1.00840
N27	0.15148	-0.02085	0.94453
O28	0.25771	0.26200	-0.11447
O29	0.64421	-0.20875	0.91613
C30	1.47478	1.16777	0.90158

6. Reference

[1] A. Laheäär, P. Przygocki, Q. Abbas, F. Béguin, *Electrochem. Commun*., 2015, **60**, 21-25.

Supporting Information for

A two-dimensional semiconducting covalent organic framework with nickel(II) coordination for high capacitive performance

Tao Li,[a] Wen-Da Zhang,[a] Yong Liu,[a] Yunxing Li,[a] Caikun Cheng,[a] Haiyan Zhu,[a] Xiaodong Yan,[a] Zaijun Li,*[a] and Zhi-Guo Gu*[ab]*

[a] *Key Laboratory of Synthetic and Biological Colloids, Ministry of Education, School of Chemical and Material Engineering, Jiangnan University, Wuxi 214122, China*

[b] *International Joint Research Center for Photoresponsive Molecules and Materials, School of Chemical and Material Engineering, Jiangnan University, Wuxi 214122, China*

E-mail: zhiguogu@jiangnan.edu.cn

1. General Information

All reagents and solvents were reagent grade, purchased from commercial sources and used without further purification. Fourier transform infrared (FT-IR) spectra were performed on a Thermo Nicolet iS10 spectrometer in the spectral range of 500-4000 cm^{-1}. ^{13}C cross-polarization with magic angle-spinning (CP-MAS) solid-state nuclear magnetic resonance (NMR) spectra were recorded on a Bruker ARX 300 MHz spectrometer. Mass spectra (MS) were taken on a Waters MALDI SYNAPT G2 Series spectrometer. X-ray photoelectron spectroscopy (XPS) analysis was measured by a Kratos Axis Supra instrument (Kratos Analytical, Manchester, UK) using a monochromatized Al Ka radiation as X-ray source. Thermogravimetric analyses (TGA) were obtained using a Mettler Toledo TGA/DSC1/1100SF analyser in the temperature range of 30 to 800 °C under flowing N_2. The Brunauer-Emmett-Teller (BET) surface areas were observed on N_2 sorption isotherms at 77 K using a Micromeritics ASAP2020 surface area and pore size analyser. Pore size distribution was determined by nonlocal density functional theory mode in the instrument software package. Scanning electron microscopy (SEM) images were obtained on a Hitachi S-4800. Transmission electron microscopy (TEM) images were observed on a JEOL JEM-2100. Scanning transmission electron microscopy (STEM) images, HRTEM images and EDS mapping were carried out on a Tecnai G2 F30 transmission electron microscopy at an acceleration voltage of 300 kV. Powder electrical conductivity was recorded on a Suzhou Jingge ST2253 by four-probe method. Thin film electrical conductivity was measured by the van der Pauw method under temperature control, the date was collected using a Keithley 4200-SCS parameter analyzer.

2. Electrochemical performance experiments

The electrochemical performances of the samples were carried out on an electrochemical station (CHI660E). Cyclic voltammetry (CV), galvanostatic charge-discharge (GCD) and Electrochemical impedance spectroscopy (EIS) measurement were conducted on in a three-electrode setup, including a Pt plate (1 cm^2) as the counter electrode and Hg/HgO electrode as the reference electrode. The working electrode was prepared by mixing active material, acetylene black and poly(tetrafluoethylene) in a mass ratio of 8:1:1, and then dispersed in ethanol by ultrasonication to obtain homogeneous slurry. The slurry was coated on a Ni foam substrate (1 cm^2). The mass loading of active materials on Ni foam was 5.0 mg cm^{-2}. Moreover, the asymmetric supercapacitor devices were assembled to test the electrochemical performance, with activated materials acting as the positive, activated carbon (AC) as the negative electrode. All the electrochemical measurements were recorded on using 3 M KOH aqueous electrolyte. EIS measurements were collected in the frequency range from 0.01 to 10^5 Hz at open circuit potential with a sinus amplitude of 5 mV.

3. Calculation Section

The specific capacitance of electrode materials was calculated by the following equation (1) and equation (2):[1]

$$E_{\text{int}/D} = I \int_{t(U_{\min})}^{t(U_{\max})} U(t)dt \quad (1)$$

$$C_{\text{int}/D} = \frac{2E_{\text{int}/D}}{U_{\max}^2} \quad (2)$$

Where $E_{int/D}$ is the energy density (Wh kg^{-1}), I is the discharge current, U is the potential range (V), t is the discharge time (s), $C_{int/D}$ is the specific capacitance (F g^{-1}). Energy density and power density of the **PG-BBT** are evaluated according to equation (3) and equation (4), respectively:

$$E = \frac{1}{2} C_{sp} V^2 \quad (3)$$

$$P = \frac{E}{\Delta t} \quad (4)$$

where E stands for the energy density (Wh kg^{-1}), C_{sp} represents the specific capacitance (F g^{-1}), V refers to the potential window (V), P is the power density (W kg^{-1}) and Δt is the discharge time (S).

4. Experimental section

Synthesis of Ni-COF

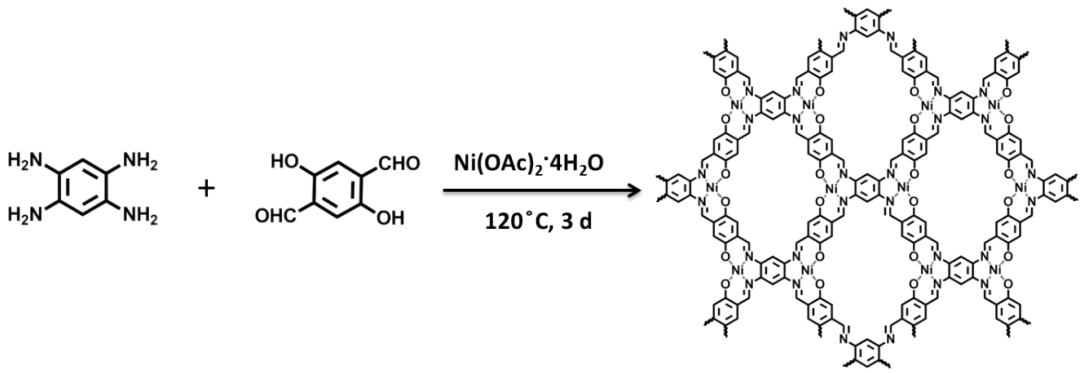

A glass bottle (volume of ca. 10 mL) was charged with 1,2,4,5-benzenetetraamine tetrahydrochloride (BTA) (20 mg, 0.07 mmol), 2,5-dihydroxy-1,4-benzenedicarboxaldehyde (HBC) (27.4 mg, 0.14 mmol), excess $Ni(OAc)_2 \cdot 4H_2O$, 0.5 mL of mesitylene and 1.5 mL of 1,4-dioxane. The resulting solution was sonicated for 10 minutes to obtain a homogenous dispersion. The glass bottle was transferred into a 25 mL Teflon-lined stainless steel autoclave. The autoclave was sealed and heated at 120 °C for 3 days and cooled to room temperature. The formed black precipitate was collected by filtration and washed with THF (3 × 20 mL), DMF (3 × 20 mL) and MeOH (3 × 20 mL), Soxhlet extracted by THF 24 h, then dried at 80 °C under vacuum for 24 h to give a black powder with 86% yield. FT-IR (powder): ν_{max} 3281, 2566, 1621, 1563, 1508, 1435, 1372, 1295, 1227, 1127, 1056, 1001, 866, 801, 676, 612 and 558 cm^{-1}.

Synthesis of Ni_0-COF

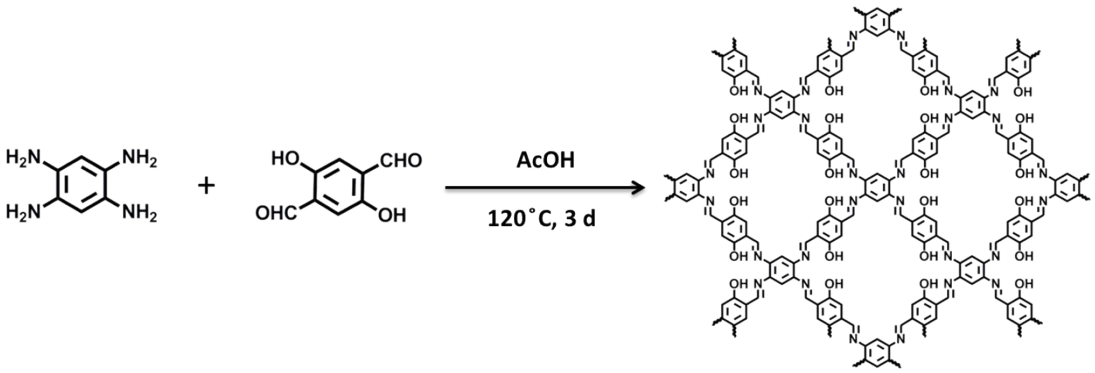

A glass bottle (volume of ca. 10 mL) was charged with 1,2,4,5-benzenetetraamine tetrahydrochloride (BTA) (20 mg, 0.07 mmol), 2,5-dihydroxy-1,4-benzenedicarboxaldehyde (HBC) (27.4 mg, 0.14 mmol), 0.5 mL of mesitylene and 1.5 mL of 1,4-dioxane. The resulting solution was sonicated for 10 minutes to obtain a homogenous dispersion, and then added 0.2 mL of 3 M aqueous acetic acid (AcOH). The glass bottle was transferred into a 25 mL Teflon-lined stainless steel autoclave. The autoclave was sealed and heated at 120 °C for 3 days and cooled to room temperature. The formed brown precipitate was collected by filtration and washed with THF (3 × 20 mL), DMF (3 × 20 mL) and MeOH (3 × 20 mL), Soxhlet extracted by THF 24 h, then dried at 80 °C under vacuum for 24 h to give a black powder with 81% yield. FT-IR (powder): ν_{max} 3072, 1621, 1576, 1492, 1431, 1358, 1281, 1258, 1202, 1157, 968, 857, 797, 743, 670 and 617 cm^{-1}.

5. Characterization

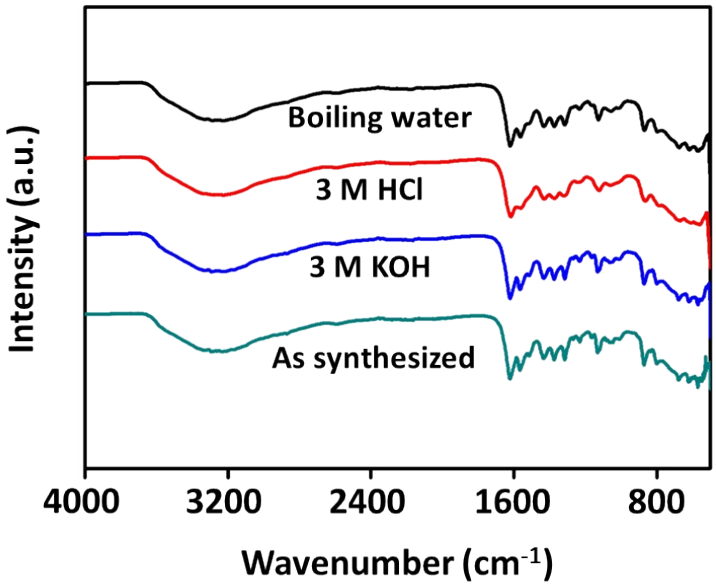

Fig. S1 Chemical stability tests of **Ni-COF**. The FT-IR patterns of **Ni-COF** treated for 5 days in different solvents.

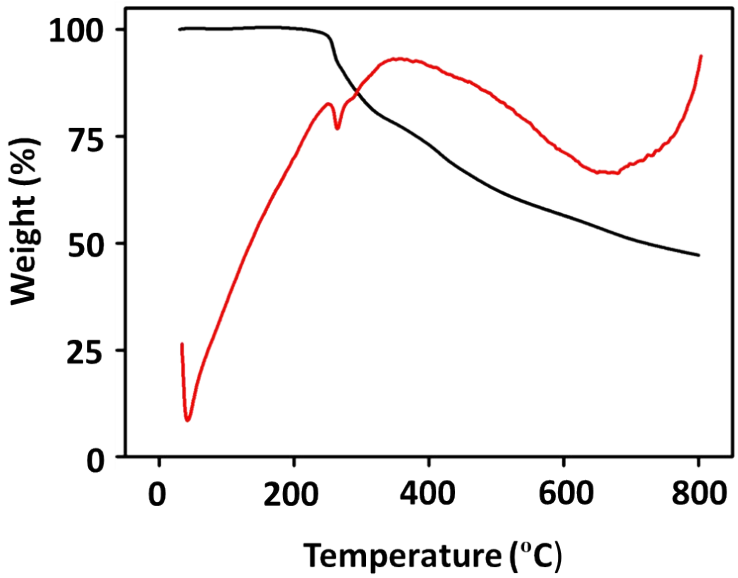

Fig. S2 Thermogravimetric analysis (TGA) curve of **Ni-COF**.

Ni-COF exhibited no discernible weight loss from 0 to 253 °C, and then **Ni-COF** started to decompose. At 800 °C, there was still 53% of weight residual for **Ni-COF**, indicating its excellent thermal stability.

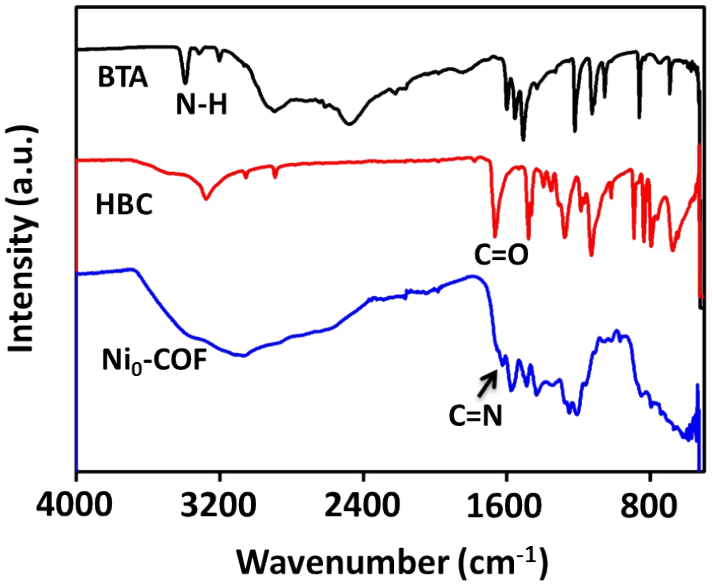

Fig. S3 FT-IR spectra of BTA, HBC and **Ni_0-COF**.

The disappearance of the characteristic C=O vibration band (1654 cm^{-1}), N-H vibration band (3389-3197cm^{-1}), and the appearance of C=N bonding (1621 cm^{-1}), indicates the formation of **Ni_0-COF**.

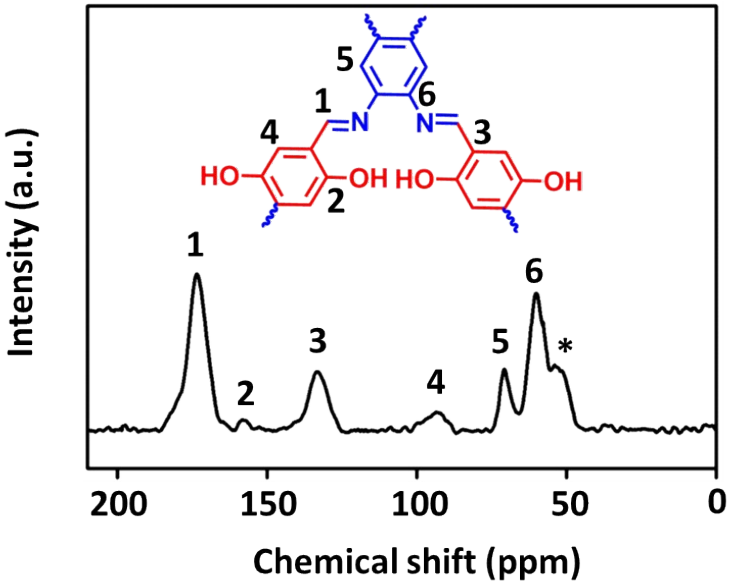

Fig. S4 Solid-state ^{13}C NMR spectrum of **Ni_0-COF**.

The characteristic resonance signal at 173 and 156 ppm is assigned to the C=N and C-O groups, respectively, which clearly reveals the formation of **Ni_0-COF**.

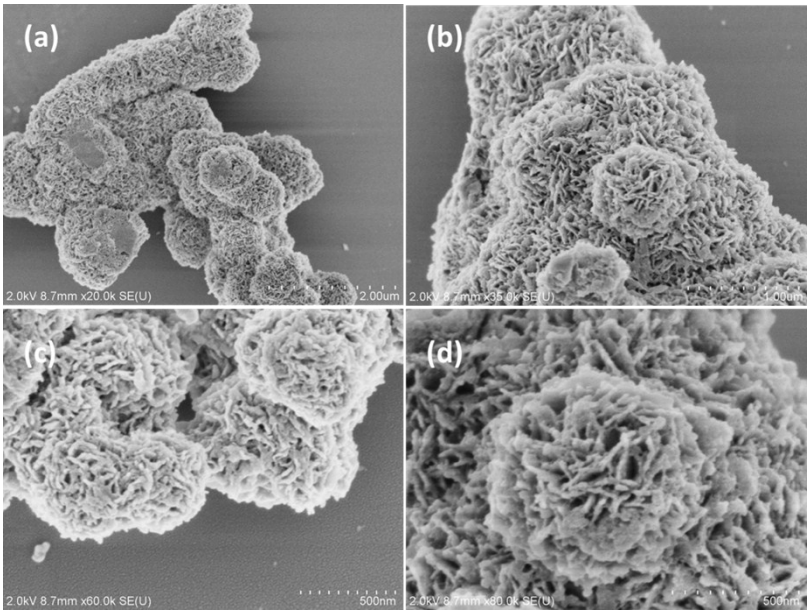

Fig. S5 SEM of **Ni-COF**.

The SEM images of **Ni-COF** show a spherical flower-like morphology, which is composed of numerous sheets.

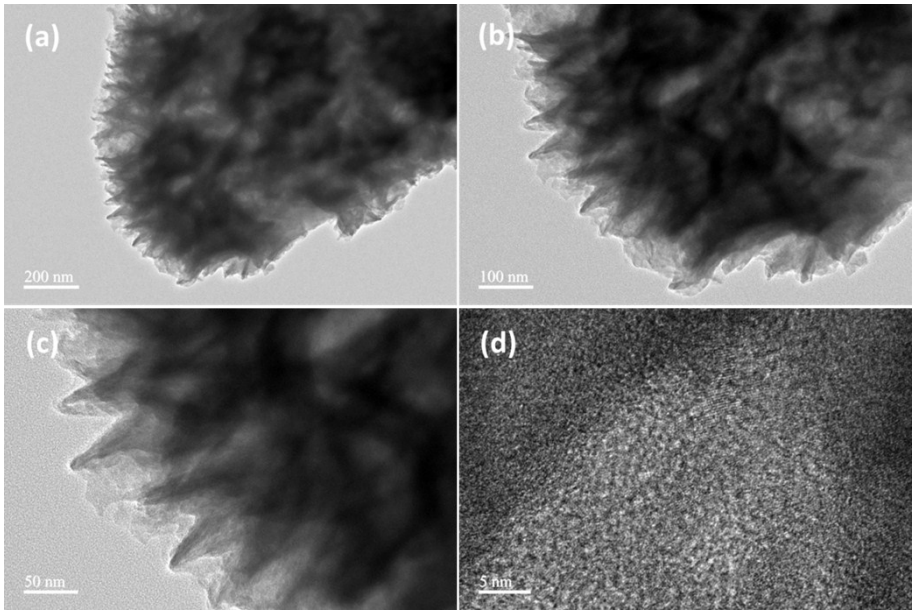

Fig. S6 TEM of **Ni-COF**.

TEM images clearly clarify that **Ni-COF** shows optically translucent feature owing to thick layer structure.

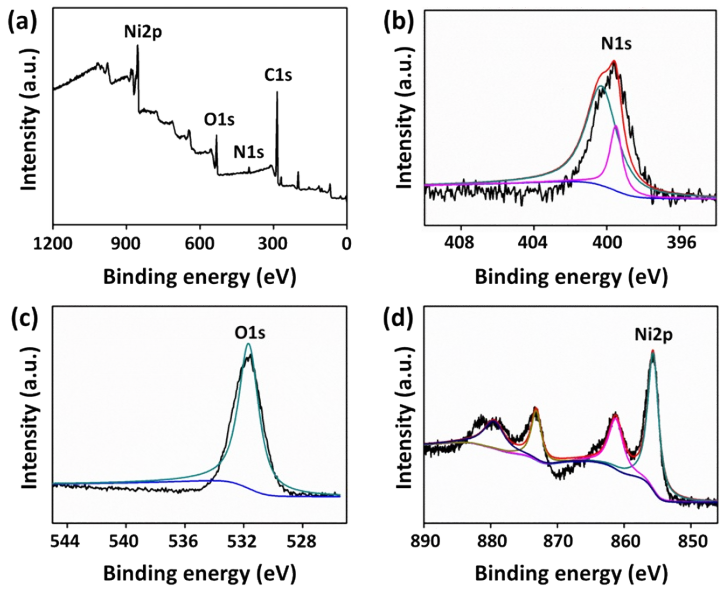

Fig. S7 XPS measurements of **Ni-COF**: (a) survey, (b) N 1s, (c) O 1s and (d) Ni 2p spectrum.

The XPS survey of Ni-COF confirms the presence of C, N, O and Ni. The signals at 399 and 532 eV correspond to N 1s and O 1s, respectively. The Ni 2p spectrum exhibits two main peaks around 856.1 and 873.6 eV that are assigned to Ni $2p_{3/2}$ and Ni $2p_{1/2}$, respectively, together with their corresponding satellite peaks around 861.3 and 880.1 eV.

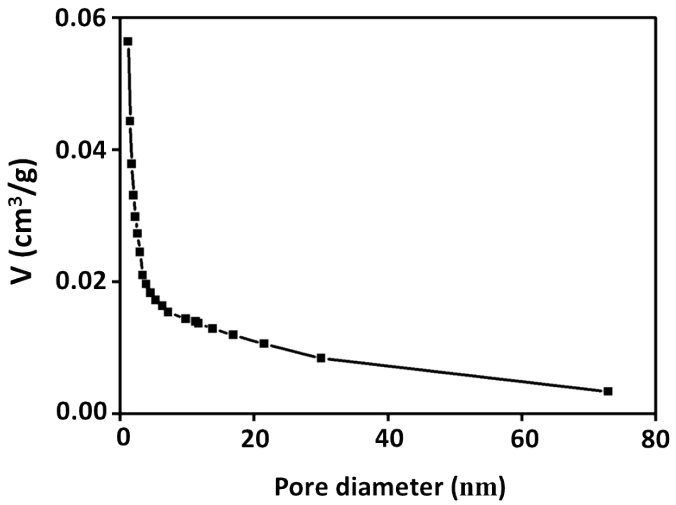

Fig. S8 Pore volume plot of **Ni-COF**.

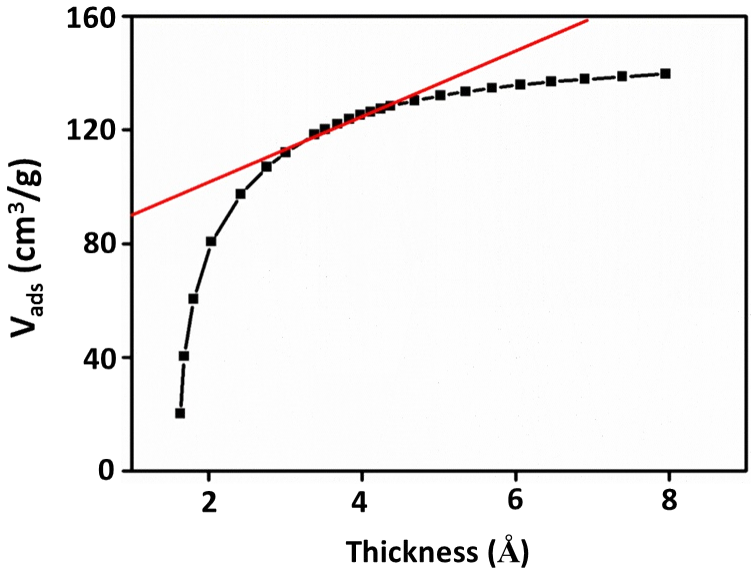

Fig. S9 t-Plots of **Ni-COF** using the Harkins and Jura reference isotherm. The lines represent the fit to the linear region, which is marked by the red symbols.

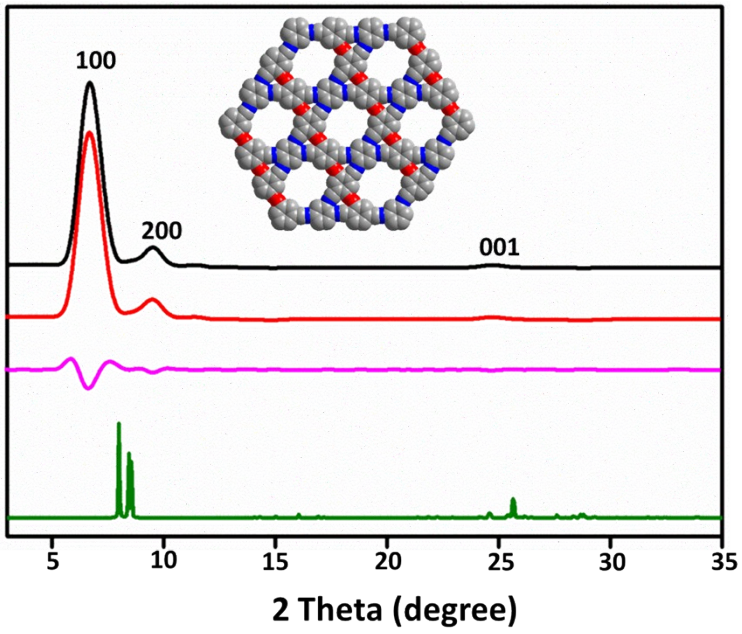

Fig. S10 PXRD patterns of **Ni_0-COF** with the experimental PXRD profiles in black, Pawley-refined profiles in red, calculated profiles in green, and the differences between the experimental and refined PXRD patterns in pink.

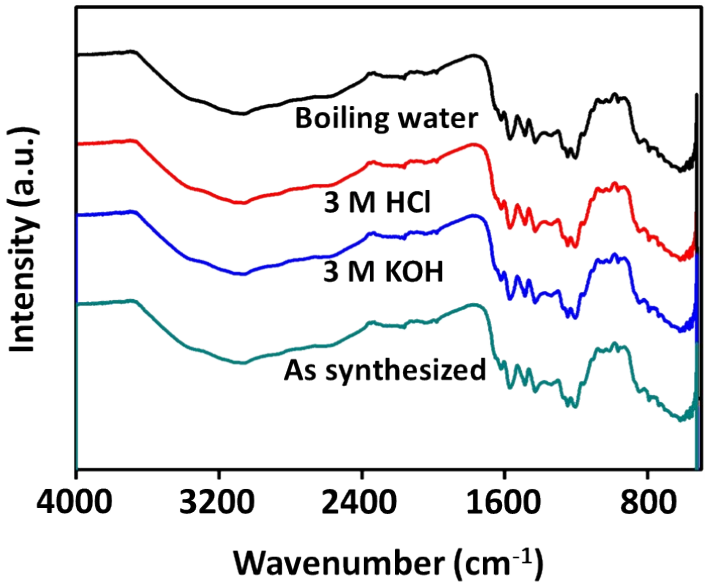

Fig. S11 Chemical stability tests of **Ni_0-COF**. The FT-IR patterns of **Ni_0-COF** treated for 5 days in different solvents.

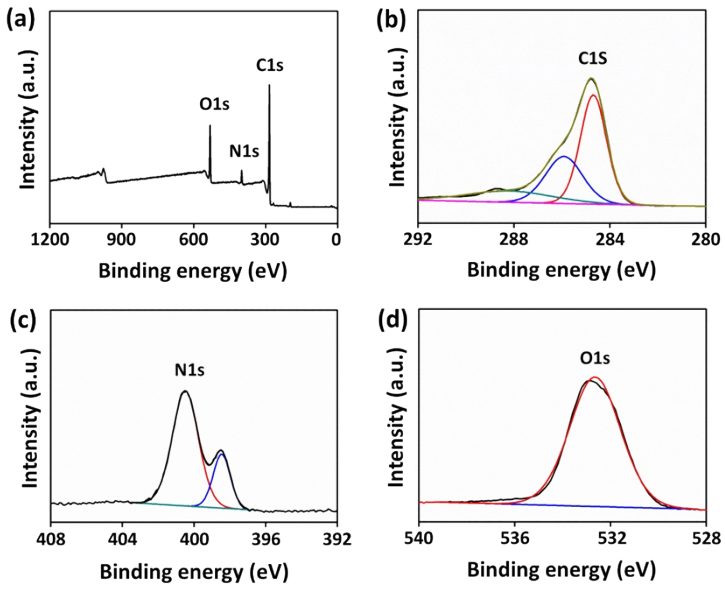

Fig. S12 XPS measurements of **Ni_0-COF**: (a) survey, (b) C1s, (c) N 1s and (d) O 1s spectra.

The XPS survey of **Ni_0-COF** confirms the presence of C, N and O. The signals at 284.8, 400.4 and 532.9 eV correspond to C1s, N 1s and O 1s, respectively.

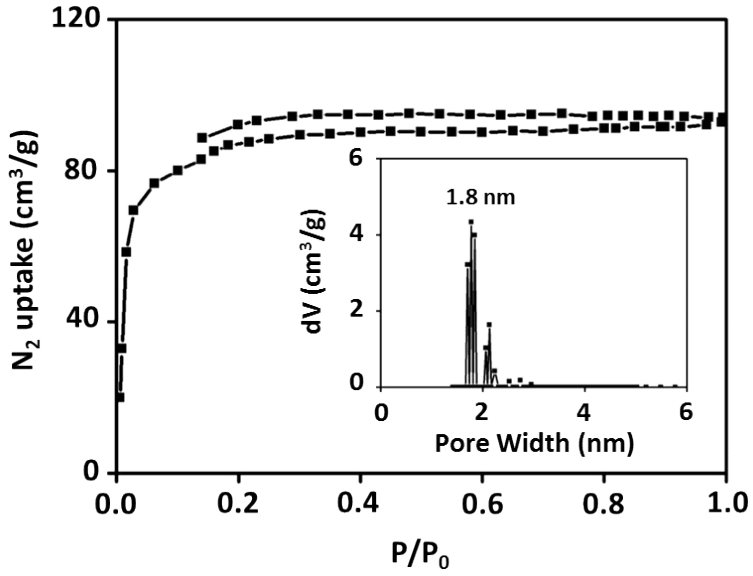

Fig. S13 Nitrogen adsorption-desorption isotherm of Ni_0-COF, and the insert exhibits the pore size distribution.

The curve displays a typical type-I shape with a sharp uptake under low relative pressure ($P/P_0 < 0.01$), indicating its microporous nature. The BET surface area of **Ni_0-COF** is estimated to be 258 $m^2 g^{-1}$. The average pore size of **Ni_0-COF** is 1.8 nm.

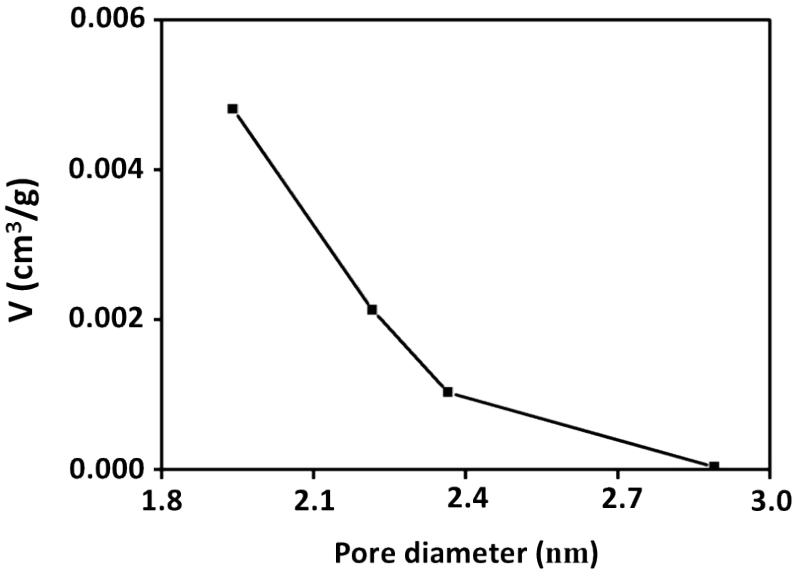

Fig. S14 Pore volume plot of **Ni_0-COF**.

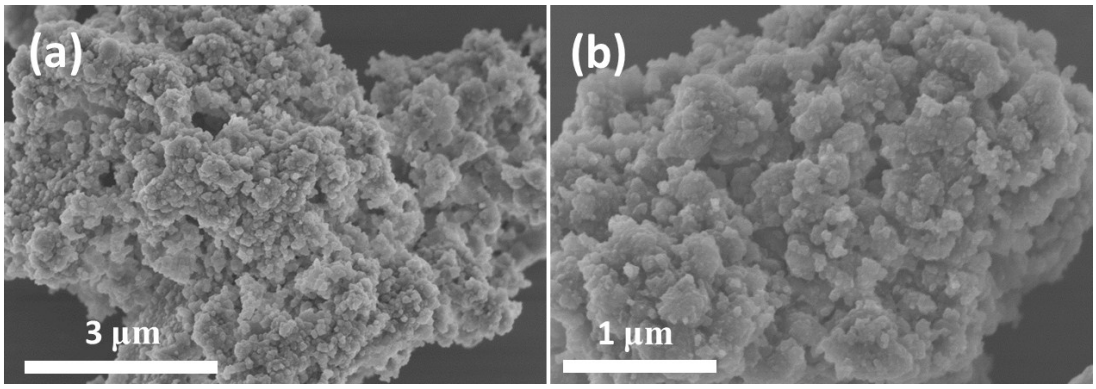

Fig. S15 SEM of **Ni_0-COF**.

The SEM images show a homogeneous morphology, which was consisted of a large number of grains.

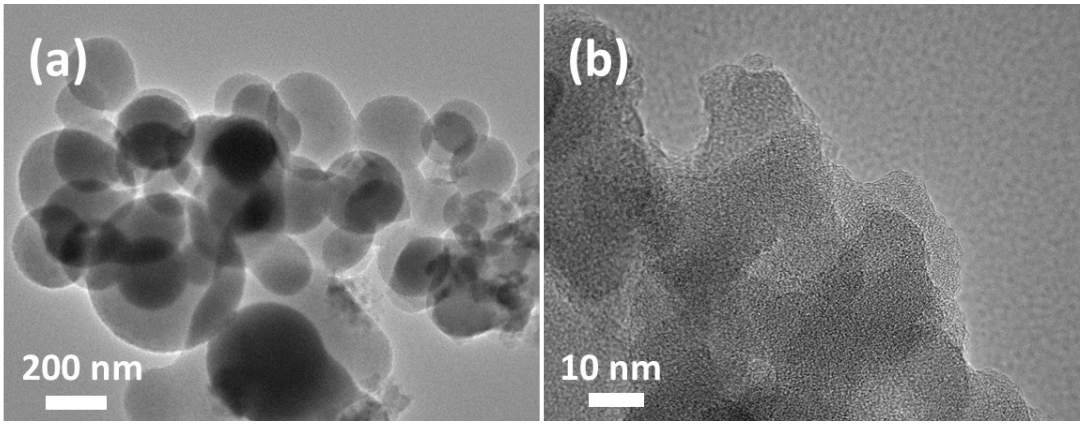

Fig. S16 TEM of **Ni_0-COF**.

The TEM images clearly observe that **Ni_0-COF** exhibits spherical grains and layer-by-layer structure.

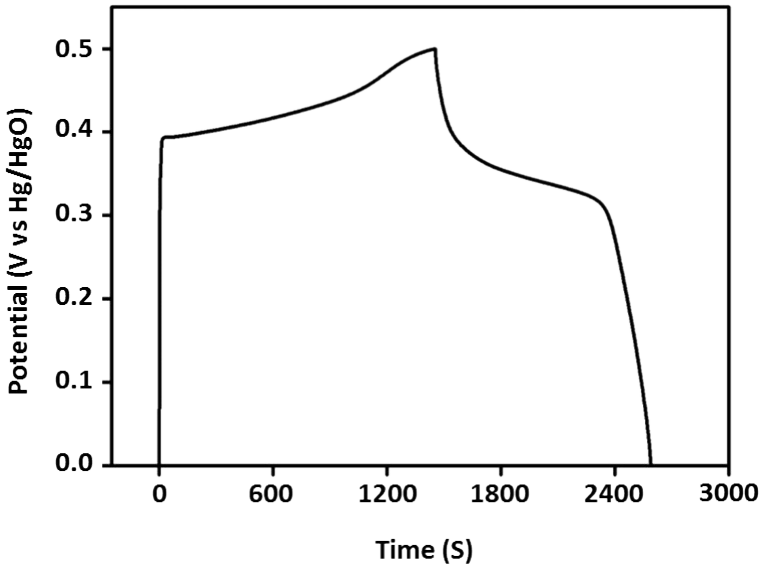

Fig. S17 GCD curve of **Ni-COF** at 0.5 A g^{-1}.

The specific capacitance of **Ni-COF** is calculated to be 1478 F g^{-1} at 0.5 A g^{-1}.

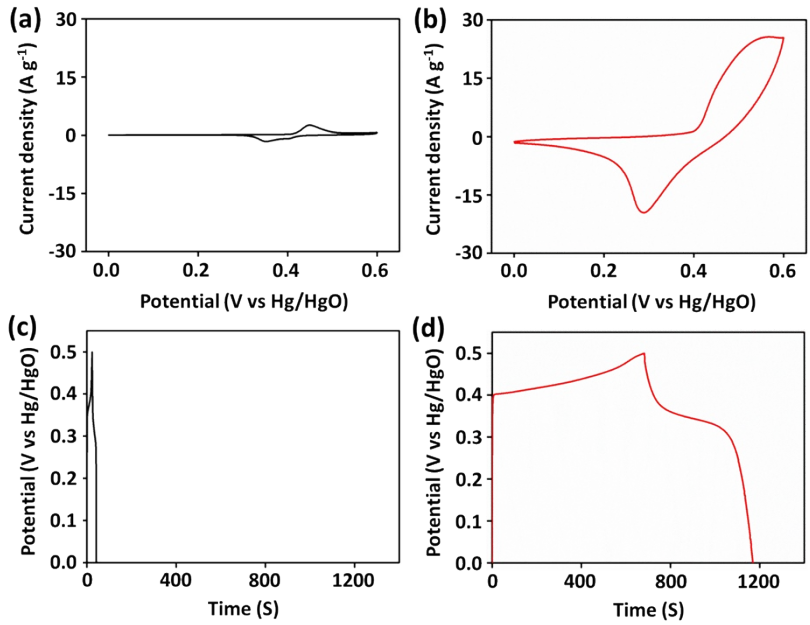

Fig. S18 CV curves of (a) Ni foam and (b) **Ni-COF** at 5 mV s^{-1}. GCD curves of (c) Ni foam and (d) **Ni-COF** at 1 A g^{-1}.

To preclude the impact of Ni foam substrate on the performance, electrochemical experiment on it was conducted (48 F g^{-1} at 1A g^{-1}). Compared with **Ni-COF** (1257 F g^{-1} at 1 A g^{-1}), the contribution from the Ni foam substrate to the total capacity is negligible.

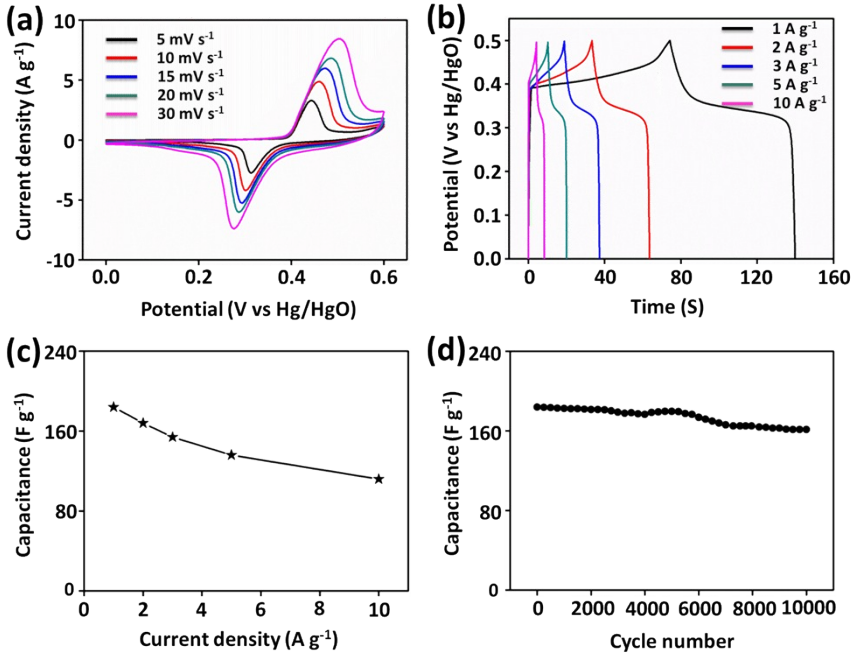

Fig. S19 Electrochemical properties of **Ni_0-COF** in a three-electrode system. (a) CV curves at scan rates from 5 to 30 mV s^{-1}. (b) GCD curves at different current densities (1-10 A g^{-1}). (c) Capacitance vs current density. (d) Cyclic stability measurement at a current density of 1 A g^{-1}.

The CV curves exhibit different scan rates from 5 to 30 mV s^{-1} and display a pair of redox peaks, indicating the pseudocapacitive behaviour. The GCD profiles show different current densities from 1 to 10 A g^{-1}. The GCD curves show a severely distorted triangular shape, which is resulted from the typical pseudocapacitive behaviour, in agreement with the CV analyses. The discharging capacitances of **Ni_0-COF** are calculated to be 184, 168, 154, 136 and 112 F g^{-1} at 1, 2, 3, 5 and 10 A g^{-1}, respectively. The specific capacitance at 10 A g^{-1} retains 61% of that at 1 A g^{-1}, indicating its good rate capability. The stability test of the **Ni_0-COF** electrode was evaluated at 1 A g^{-1}. It demonstrates high stability with high capacitance retention of 87.5 % after 10000 cycles.

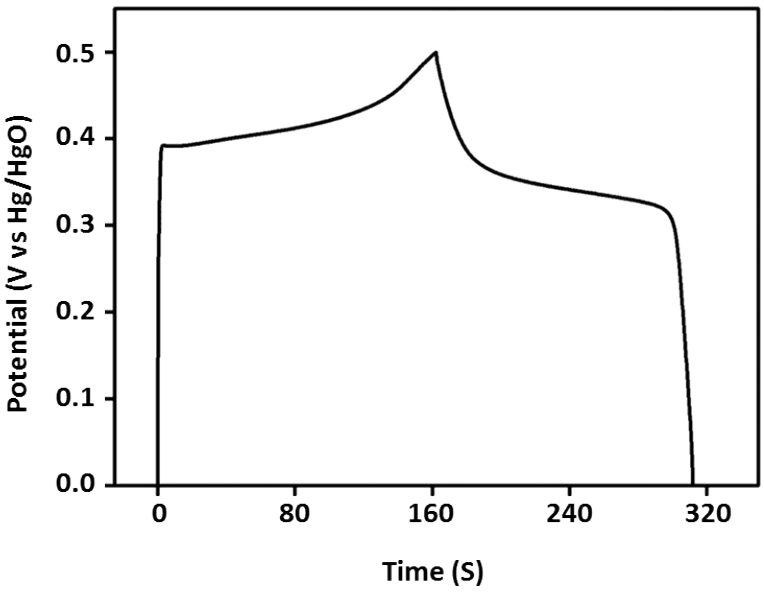

Fig. S20 GCD curve of **Ni_0-COF** at 0.5 A g^{-1}.

The specific capacitance of **Ni_0-COF** is calculated to be 204 F g^{-1} at 0.5 A g^{-1}.

Table S1. Fractional atomic coordinates for the triclinic *P*1/(1) unit cell of **Ni-COF** calculated using the Materials Studio 7.0.

Ni-COF			
Triclinic *P*1/(1) *a* = 12.8777 Å, *b* = 12.1493 Å, *c* = 14.8164 Å			
C1	1.12607	1.09325	-0.34932
C2	0.19516	1.04500	-0.28450
C3	0.08888	0.01325	0.89411
C4	-0.08759	0.01475	0.01845
C5	0.83769	0.05471	-0.03641
C6	0.95110	1.09874	-0.22850
N7	-0.19843	-0.05550	0.23180
C8	-0.30027	0.05432	1.25405
C9	-0.14787	0.28604	1.06463
C10	0.06568	0.38215	-0.10817
C11	0.19392	0.60524	0.71894
C12	0.11821	0.73890	0.70731
C13	-0.09166	0.64556	0.87511
C14	-0.22250	0.41979	1.05298
C15	0.20979	0.90225	0.61688
N16	0.18645	1.08387	0.52606
O17	0.15807	0.26699	-0.11881
O18	-0.18603	0.75377	0.89622
N19	0.18645	0.11717	-0.27905
C20	0.67973	0.05196	0.89536
C21	0.59246	0.03926	0.87628
C22	0.34446	-0.09644	0.13816

C23	0.24332	-0.12747	1.14688
C24	0.39008	-0.03002	0.89774
C25	0.64095	0.11375	0.62821
C26	0.74477	0.15176	0.61286
C27	0.26786	-0.12468	0.95940
N28	0.13234	-0.04848	0.99266
Ni29	1.08812	0.19514	0.43073
O30	-0.01515	-0.29032	0.43887
O31	1.00377	0.31728	0.31835
Ni32	1.89884	1.83119	1.32795

Table S2. Fractional atomic coordinates for the triclinic P1/(1) unit cell of **Ni_0-COF** calculated using the Materials Studio 7.0.

Ni_0-COF			
Triclinic P1/(1) *a* = 12.9144 Å, *b* = 12.4401 Å, *c* = 22.1318 Å			
C1	1.02688	0.82450	-0.08070
C2	0.09651	0.81008	-0.05189
C3	0.07812	-0.08066	0.95399
C4	-0.01143	0.06066	-0.07444
C5	0.90331	0.07226	-0.09593
C6	0.91337	0.94356	-0.09096
N7	-0.00042	0.18851	-0.09024
C8	-0.05438	0.35796	0.86442
C9	-0.02392	0.47331	0.85173
C10	0.07117	0.42719	-0.12226
C11	0.12044	0.57646	0.84158
C12	0.01958	0.71919	0.82860
C13	-0.06181	0.77289	0.79567
C14	0.08956	0.66065	0.79993
C15	0.10287	0.66450	0.86234
N16	-0.01906	0.77279	0.90680
O17	0.14064	0.27534	-0.08742
O18	-0.11796	0.92781	0.76363
N19	-0.18548	-0.06899	-0.09161
C20	0.71214	0.04998	0.88960
C21	0.58584	0.02849	0.90778
C22	0.33677	0.15746	0.91906

C23	0.28979	-0.00167	0.96692
C24	0.27058	-0.27046	1.11021
C25	0.52734	-0.12813	0.95580
C26	0.19029	-0.09786	1.00840
N27	0.15148	-0.02085	0.94453
O28	0.25771	0.26200	-0.11447
O29	0.64421	-0.20875	0.91613
C30	1.47478	1.16777	0.90158

6. Reference

[1] A. Laheäär, P. Przygocki, Q. Abbas, F. Béguin, *Electrochem. Commun*., 2015, **60**, 21-25.